Title
Optical Simulation and Design of a Virtual Reality Headset for Retinal Imaging

Author
Bharadwaj, Gautama

Publication Date
2023

Peer reviewed|Thesis/dissertation

Optical Simulation and Design of a Virtual Reality Headset for Retinal Imaging

By

GAUTAMA BHARADWAJ
THESIS

Submitted in partial satisfaction of the requirements for the degree of

MASTER OF SCIENCE

in

Electrical and Computer Engineering

in the

OFFICE OF GRADUATE STUDIES

of the

UNIVERSITY OF CALIFORNIA

DAVIS

Approved:

Iman Soltani

Soheil Ghiasi

Erkin Seker

Committee in Charge

2023

Contents

List of Figures

List of Tables

Abstract

Hundreds of millions of people worldwide are affected by visual disabilities, due to various factors, including genetics, injury, infection, or aging. Majority of visual impairment are avoidable with timely intervention and early detection. The high prevalence of avoidable visual impairment is primarily due to underutilization of eye care services, stemming from challenges related to availability, accessibility, and affordability. Inadequate numbers of trained professionals pose a significant obstacle in expanding access to eye care services, particularly in rural areas with higher demand. Additionally, individuals with disabilities, and those facing financial and socioeconomic barriers encounter greater challenges in accessing eye care services, further exacerbating the issue.

Ocular imaging modalities, such as Optical Coherence Tomography (OCT) and fundus imaging, are vital for diagnosing retinal diseases. OCT generates high-resolution images of the retina, enabling early detection of abnormalities, while fundus imaging captures photographs of the eye's back, useful for screening retinal diseases. However, clinical OCT systems are large and require dedicated space, limiting their use in compact or field settings. Patients may also face challenges due to the need for head stabilization, especially those with movement difficulties or individuals with mental, physical or developmental disabilities.

A virtual reality (VR)-based headset that can perform multi-modal retinal imaging is designed, specifically OCT and scanning laser ophthalmoscopy. The headset is designed to be worn by patients while watching videos, enabling the simultaneous capture of OCT and fundus images. The project aims to overcome limitations by eliminating the requirement for mechanical head stabilization and skilled operators. Moreover, the use of portable VR headsets can enhance the affordability of eye care by reducing the need for dedicated space and trained professionals, and potentially introducing automation for image capture and diagnosis. Optical simulations are performed to test the performance of the proposed system in terms of retinal coverage and resolution. The feasibility of pupil tracking and the ability to control the user's gaze to improve optical performance is tested.

Acknowledgments

I would like to express my gratitude and appreciation to all those who have contributed to the successful completion of my master's thesis.

First and foremost, I would like to thank Dr. Iman Soltani, for providing me with numerous opportunities that have been critical for my growth and development academically, professionally and on a personal level. The opportunities and the platform that the lab provided me with, have allowed me to give my best towards research. I am extremely grateful for the mentorship and guidance that I have received from him throughout these two years. I appreciate the transparent and honest feedback that I have always received, regardless of it being personal or research-related.

I would like to express my gratitude to my committee members Dr. Soheil Ghiasi and Dr. Erkin Seker for their valuable feedback and guidance.

I would like to thank and acknowledge Dr. Soundararajan, Adithya, Victoria, Jiamin, Nathan and Vamsi who have all contributed to the work presented in this thesis. I am also grateful to everyone at LARA Lab for creating a supportive environment and culture, which has contributed to my personal and professional growth. I have enjoyed my interactions with all the people at the lab and would like to express my gratitude for their contributions to my experience.

Lastly, I would like to thank my family for unwavering support and love without which I would not be where I am. I would also like to offer a special thanks to Deepa for being my emotional support system and helping me get through all sorts of thick and thin.

CHAPTER 1

Introduction

1.1. Global Magnitude of Vision Impairment

Visual disabilities are a major health concern affecting millions of people worldwide. They can be caused by a variety of factors such as genetics, injury, infection, or aging. Visual disabilities can have a profound impact on a person's quality of life, ability to work, and overall well-being. While there are numerous eye defects resulting in visual disabilities, the severity of vision impairment is broadly classified into mild, moderate, severe, blindness and near vision impairment based on a non-invasive measure of the visual system's ability to discriminate two high contrast points in space [**5**].

Vision Loss Expert Group in 2015 reported that, among a population of 7.33 billion individuals, approximately 36 million people were blind, while around 216.6 million had moderate to severe visual impairment and 188.5 million had mild impairment [**6**]. A further analysis of the causes of blindness and moderate to severe visual impairment is shown in Table 1.1 reproduced from data estimates from a second paper published by the group [**3**, **4**].

Cause	**Blind**		**Moderate-severe**		**All impairment**	
	Millions	**%**	**Millions**	**%**	**Millions**	**%**
Cataract	12.6	35	52.6	24	65.2	26
Uncorrected refractive error	7.4	21	116.3	54	123.7	49
Glaucomas	3	8	4	2	7	3
Age-related macular degeneration	2	5	8.4	4	10.4	4
Corneal opacity	1.3	4	2.9	1	4.2	2
Trachoma	0.4	1	1.6	1	2	1
Diabetic retinopathy	0.4	1	2.6	1	3	1
All other causes	8.9	25	28.2	13	37.1	14
Total	**36**	**100**	**217**	**100**	**253**	**100**

TABLE 1.1. Prevalence of visual impairment by cause [**3**, **4**]

While the definition of avoidable vision loss is subjective, cataract and uncorrected refractive error are widely accepted as types of vision loss that are treatable or preventable, since cataract can be surgically treated and uncorrected refractive error can be corrected with spectacles or contact lenses. Although it is uncertain whether age-related macular degeneration (AMD), glaucoma, and diabetic detinopathy (DR) can be classified as treatable or preventable, as the amount of preventable or treatable vision loss is unclear [**7**], timely intervention and early detection can help prevent most cases of vision impairment caused by diabetic retinopathy and glaucoma [**5**].

The Vision Loss Expert Group defines avoidable vision loss due to a preventable or treatable cause as any vision loss due to cataract, uncorrected refractive error, trachoma, glaucoma, diabetic retinopathy, or corneal opacity. According to this definition, in 2015, 205.1 million cases out of 252.6 million with blindness or moderate to severe visual impairment were avoidable [**3**].

Analogous to Table 1.1, World Health Organization (WHO) estimates that 11.9 million people globally have moderate or severe vision impairment or blindness due to glaucoma, diabetic retinopathy and trachoma that could have been prevented. WHO also reports that preventing vision impairment in the estimated 11.9 million individuals would have incurred a cost of approximately US$32.1 billion [**5**].

The high prevalence of avoidable visual impairment can be attributed to the inadequate utilization of eye care services, which can be attributed to factors such as the availability, accessibility, and affordability of such services. The impact of these factors are briefly discussed below.

- **Availability:** The inadequate number of trained professionals presents a significant obstacle in expanding access to eye care services and addressing preventable vision impairment and blindness. Although it is essential to ensure that the eye care workforce is distributed according to population needs, many countries exhibit an uneven allocation of trained eye care professionals. Rural areas, in particular, have a higher demand for eye care services relative to the limited number of professionals available. [**8**, **9**, **10**].
- **Accessibility:** Research has shown that women face greater challenges in accessing eye care services due to financial, socioeconomic, and cultural factors, resulting in unequal access to such services [**11**, **12**, **13**]. Studies also show that people with physical, mental and intellectual disabilities face steeper challenges in accessing eye care services [**14**,**15**,**16**].

- **Affordability:** Affordability of eye services depends heavily on the economic ability of the individual to afford costs such as eye care, transportation and pharmaceutical necessities amongst other things.

1.2. Problem statement

Ocular imaging modalities, such as fundus imaging and optical coherence tomography (OCT), are important diagnostic tools used in ophthalmology to evaluate and diagnose a wide range of retinal diseases. OCT is a non-invasive optical imaging technique based on low-coherence interferometry that utilizes broadband light sources to generate high-resolution and high-definition three-dimensional (3D) images of biological tissue. This imaging modality allows for a detailed evaluation of retinal structures and can detect abnormalities in the early stages of diseases. Fundus imaging, on the other hand, involves capturing a photograph of the eye, including the retina, optic disc, and blood vessels. It is commonly used for screening and monitoring of retinal diseases such as diabetic retinopathy, age-related macular degeneration, and glaucoma.

Both OCT and fundus imaging provide valuable information for diagnosis and management of various retinal diseases, and their combination in a multi-modal imaging device could enhance the accuracy of diagnosis and improve patient care.

While OCT and fundus imaging are an indispensable components of diagnostic imaging for almost all ophthalmic diseases, the clinical OCT systems are table-top or floor-standing instruments that require a dedicated space in a clinical setting, which limits their use in field settings or in locations with limited space.

Additionally, mechanical head stabilization, such as a chinrest or forehead brace, is needed to position the head, align the eye, and suppress motion, as it requires the patient to remain motionless during the entire imaging process. This can be challenging for some patients, especially those who have difficulty holding their head still or who have medical conditions that make it difficult to maintain a fixed position - patients with mental and developmental disabilities such as autism, for example.

Finally, trained ophthalmic photographers are also necessary for operating clinical OCT systems, which prevents many population groups that can benefit from this technology due to the uneven allocation of trained eye care professionals around the globe. Figure 1.1 shows a typical clinical OCT setup that requires a trained professional and instructional patient protocol.

FIGURE 1.1. Traditional OCT machines require skilled technicians and patients need to be able to sit at the machine and follow instructions.

The accessibility constraints due to the large table-top instrumentation required, unequal distribution of eye care professionals, and the logistics of the eye scan concerning head stabilization prevent a large chunk of the population from receiving eye services that can be crucial in preventing and curing eye diseases. The constraints of the current clinical solution highlight the need for ocular imaging technologies that are easily accessible to all patients regardless of age, socio-economic background, or mental/physical health.

1.3. Previous work

There have been attempts to address the limitations of ocular imaging in the form of handheld, portable devices that perform OCT or Fundus imaging [**17**, **18**, **19**, **20**, **21**]. While these portable devices are helpful for a subset of patients such as infants or bedridden adults, these devices continue to be heavily dependent on experienced operators who can guide the instrument precisely through the patient's pupil. The images captured with a handheld probe may also exhibit motion artifacts due to the movement of the examiner and/or the child, which affects the quality of imaging. The unavailability of experienced eye care professionals continues to be a problem, even for such handheld imaging devices. Additionally, handheld devices still require the patients to maintain a fixed gaze towards the instrument, making it nearly impossible to use on younger toddlers or patients with more severe neurodevelopmental disorders like autism [**22**]. For these patients, imaging can only be done while they are under anesthesia [23]. However, due to the side effects and practical difficulties associated with sedation, these imaging procedures are often avoided unless absolutely necessary, leading to many pathologies going undiagnosed until it is too late. To date, academic and industry efforts have failed to make ocular imaging widely accessible to all patients. Recently, an autonomous robot-mounted OCT scanner has been developed that utilizes robotic positioning to align with the eye to be imaged, eliminating the need for operator intervention or head stabilization [24].

1.4. Current work

This thesis discusses the development of a virtual reality (VR)-based headset capable of performing multi-modal retinal imaging, specifically OCT and scanning laser ophthalmoscopy. The headset is intended to be worn by the patient or user while watching videos, enabling simultaneous capture of OCT and fundus images. The goal of this project is to address the limitations identified in the previous section through several means:

- **Availability:** As the patient wears the headset and watches a video while the optical system captures the OCT and fundus images simultaneously, mechanical head stabilization in the form of chinrest or the requirement of remaining completely still is not needed. If the patient moves their head, the optics move with them, thereby, the limitation of mechanical alignment is resolved. As the capturing of OCT and fundus can be automated, this setup reduces the dependency on the skillset of the operator, thereby addressing the problem of availability of trained eye care professionals around the globe.
- **Accessibility:** Studies show positive signs when it comes to the usage of virtual reality in the treatment of intellectual and developmental disabilities, such as autism [25, 26]. These promising studies show that using virtual reality headsets for retinal imaging and addresses the gaps in the accessibility of eye care for people with physical, mental and intellectual disabilities.
- **Affordability:** Clinical OCT currently requires access to a dark room and dedicated space; it cannot currently be used in spaces with limited space. Additionally, the requirement of a dedicated space for performing OCT requires a lot of money. By using

a portable VR-based headset as an alternative to a table-top setup, the cost of eye care will be significantly reduced. Another major cost to eye care is the involvement of trained professionals to operate the large table-top instruments. By automating image capture, and in the future, diagnosis, we can address the issue of high operating costs of OCT.

1.5. Thesis organization

The remainder of the thesis is organized as follows:

- Chapter 2 outlines the basics of retinal anatomy, diseases, and the techniques of OCT and Fundus imaging.
- Chapter 3 deals with the design, simulation, and performance validation of the optical system.
- Chapter 4 discusses the pupil movement characteristics and experiments conducted to validate the feasibility of the design.
- Chapter 5 concludes the thesis and discusses the limitations of the current design and elaborates on future work.

CHAPTER 2

Background

2.1. Anatomy of the eye

The anatomy of the eye can be described as a spherical structure filled with fluid and enclosed by three layers of tissue. The outermost layer is composed mainly of the sclera, a tough white fibrous tissue that transforms into the transparent cornea at the front of the eye. The middle layer of tissue comprises the iris, the ciliary body, and the choroid, which are three distinct structures that form a continuous ring. The iris, which is the visible colored part of the eye, contains muscles that regulate the size of the pupil under neural control. The ciliary body encircles the lens and includes a muscular component that adjusts the lens's refractive power and a vascular component that produces the fluid in the front of the eye. The choroid supplies the photoreceptors of the retina with a rich capillary bed of blood. Finally, the innermost layer of the eye, the retina, contains neurons that are sensitive to light and transmit visual signals to central targets [**27**]. Figure 2.1 shows the anatomy of the eye and the layers and the organization of the retina [**28**].

The retina, a light-sensitive tissue located at the back of the eye, consists of several distinct layers. Starting from the outermost layer, there is the photoreceptor layer, which contains specialized cells called rods and cones that capture light and initiate the visual signal. The signals then pass through the bipolar cell layer, where they are modulated and transmitted to the ganglion cell layer. Ganglion cells serve as the output neurons of the retina and transmit visual information to the brain via the optic nerve. Between these layers, there are also interneurons such as horizontal cells and amacrine cells, which play crucial roles in processing and integrating visual signals. The complex interactions between these layers and their respective cells contribute to the formation and transmission of visual information from the retina to the brain, enabling the perception of the surrounding visual world. The central part of the retina, called the macula, is responsible for sharp, detailed vision, while the peripheral retina is responsible for peripheral vision.

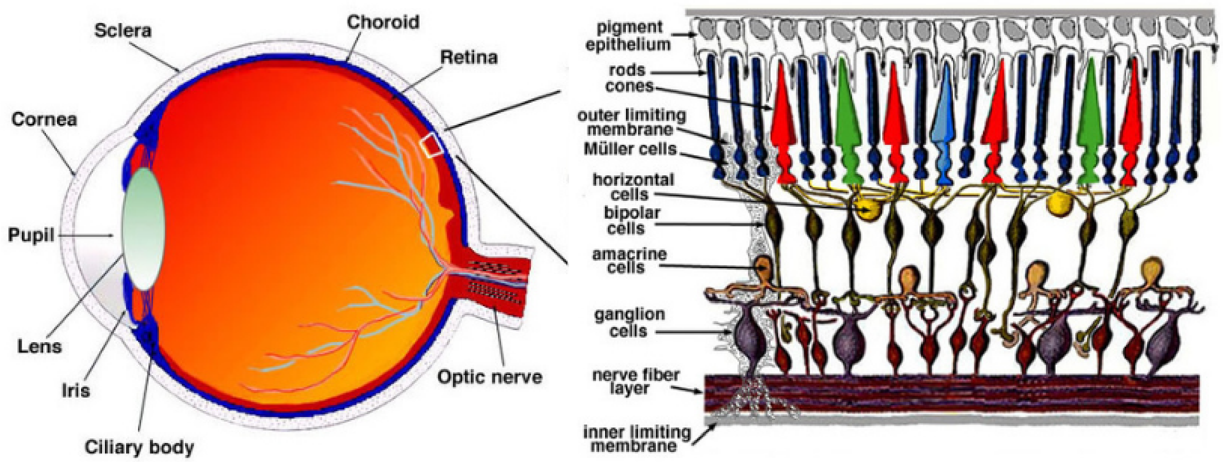

FIGURE 2.1. The anatomy of the eye with a schematic enlargment of the retinal layers.

2.2. Retinal Diseases

Amongst the most prevalent causes of visual impairment mentioned in Table 1.1, glaucoma, age-related macular degeneration and diabetic retinopathy are all diseases related to the retina and was estimated to be the cause of blindness or moderate to severe visual impairment for 20.4 million people in 2015 [**6**]. A brief overview of these diseases are as follows:

- **Glaucoma:** Glaucoma is a group of eye diseases that affect the optic nerve, which is responsible for transmitting visual information from the eye to the brain. It is characterized by the progressive degeneration of the optic nerve, leading to visual impairment [**29**]. The distinctive feature of glaucoma is the cupping of the optic disc, which is visually manifested in the 3-D structure of the optic nerve head (ONH) [**30**]. ONH imaging using techniques such as OCT and scanning laser ophthalmoscopy (SLO) that can provide detailed structural information about the optic nerve and help in the detection of glaucoma. Glaucoma can be treated through various modalities such as medications, laser therapy, and surgery. Early diagnosis and treatment can prevent vision loss from the disease [**31**].
- **Age-related macular degeneration (AMD):** AMD is a chronic and progressive disease affecting the macula, which is the central region of the retina responsible for high-acuity vision. Vision loss in age-related macular degeneration occurs mainly in the advanced stages

of the disease which can be categorized into two types: neovascular (or "wet") age-related macular degeneration and geographic atrophy (or "late dry"). Neovascular age-related macular degeneration is caused by choroidal neovascularization that breaches the neural retina, resulting in fluid, lipid, and blood leakage leading to fibrous scarring. In geographic atrophy, progressive degeneration of the retinal pigment epithelium, choriocapillaris, and photoreceptors occurs. Retinal imaging through OCT allows for early detection and monitoring of AMD. Fundus fluorescein angiography and indocyanine green angiography may also be used to detect abnormal blood vessels that occur in neovascular AMD [**32**]. The treatment of advanced AMD depends on the type of the disease. Anti-VEGF therapy can be used to treat neovascular AMD. Photodynamic therapy and laser surgery are other treatment options for destroying abnormal blood vessels [**33**].

- **Diabetic retinopathy (DR):** DR is a complication of diabetes mellitus that affects the blood vessels in the retina [**34**]. In the early stages of diabetic retinopathy, the blood vessels may leak fluid or small amounts of blood into the retina, leading to swelling and distorted vision. As the disease progresses, the blood vessels may become blocked, depriving the retina of oxygen and nutrients, and causing the growth of new abnormal blood vessels. Diabetic retinopathy can be diagnosed through a comprehensive eye examination that includes a visual acuity test, pupil dilation, and a dilated eye exam. In addition, the eye doctor examines the retina and optic nerve for signs of damage and in some cases, a fluorescein angiography or an OCT may also be performed.

Diagnosis of these retinal diseases depends on the OCT and fundus imaging amongst other modalities to capture the retinal image. In addition to ocular and retinal diseases, retinal imaging enables the identification, diagnosis, and management of cardiovascular and hypertensive diseases [**35**].

2.3. History of retinal imaging

The history of retinal imaging goes back to the early 19th century when scientists first began to explore the use of optics in medicine. The principles of the ophthalmoscope were first invented by Czech scientist Jan Evangelista Purkyně in 1823 and were later reinvented by Charles Babbage

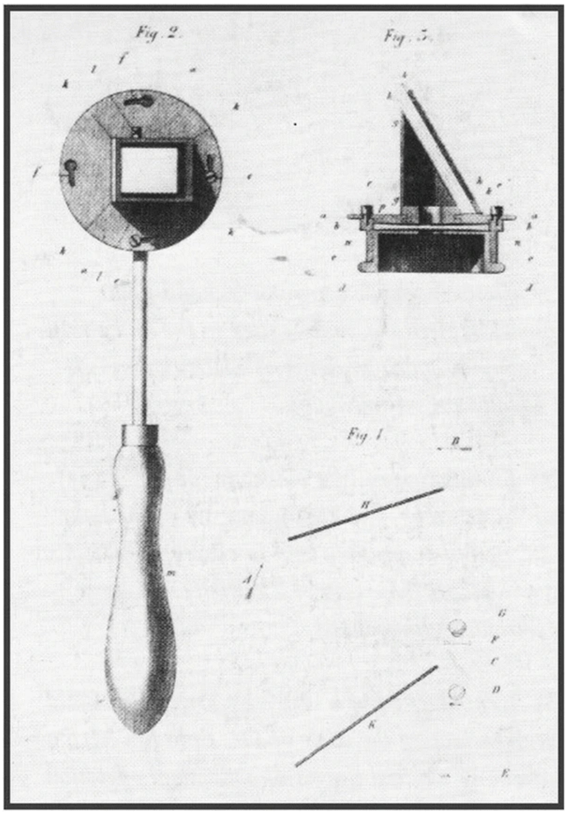

(a) Early ophthalmoscope as designed by Helmholtz

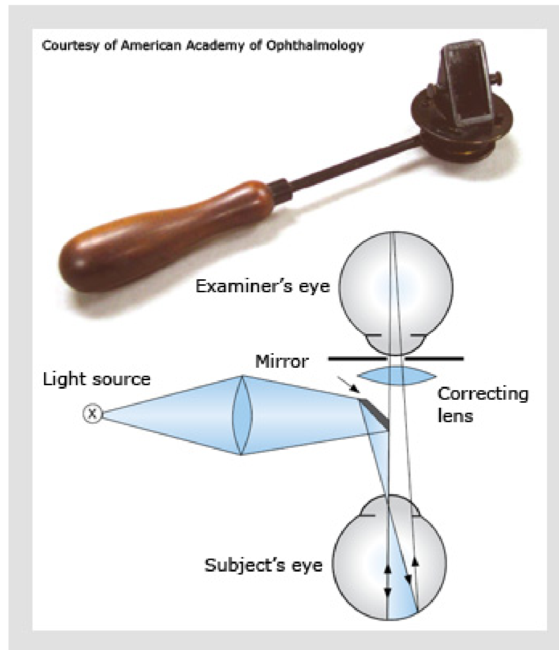

(b) Light path for the original ophthalmoscope

FIGURE 2.2. Early ophthalmoscope invention and idea [**1**]

in 1845 [**36**,**37**]. In 1851, von Helmholtz reinvented the ophthalmoscope, which allowed for routine inspection and evaluation of the retina by ophthalmologists [**36**]. The early ophthalmoscope and the light path in the design by Helmholtz is shown in Figure 2.2 [**1**].

Due to the high incidence of infectious diseases during that era, and the proximity of the physician to the patient's face required for using an ophthalmoscope, photography of the eye became a desirable alternative. The fundus camera, which is still employed for retinal imaging today, was introduced by Gullstrand in 1910, for which he was later awarded the Nobel Prize [**36**]. The subsequent significant progress was made with the creation of fluorescein angiographic imaging. It employs a fundus camera with specialized narrow band filters to capture images of a fluorescent dye introduced into the bloodstream, which adheres to white blood cells [**38**].

One limitation of fundus imaging is that it only provides a two-dimensional image of the retina, making it difficult to accurately measure the thickness of different retinal layers. OCT, which allows for 3D imaging, addressed these limitations. OCT is a non-invasive imaging technique that uses low-coherence interferometry to create a three-dimensional, high-resolution image of the retina. This allowed for more accurate measurements of retinal thickness and the identification of subtle changes in retinal structures.

2.4. Imaging modalities

Retinal imaging mainly employs two modalities: Fundus Imaging and Optical Coherence Tomography. Additionally, there are other imaging techniques such as Fluorescein angiography and OCT angiography that are built on principles of Fundus Imaging and OCT.

2.4.1. Fundus imaging and scanning laser ophthalmoscopy (SLO). Fundus imaging is a non-invasive diagnostic technique that uses a specialized camera to capture images of the retina, optic disc, and blood vessels at the back of the eye. Fundus photography can be performed with colored filters, or with specialized dyes including fluorescein and indocyanine green.

SLO is a technique that uses a laser beam to scan the retina and create a high-resolution image. While the usage of SLO has been limited to sub-specialty clinics, the high-resolution, better contrast and wider field of view makes it an important technique.

Figure 2.3 shows the comparison between a fundus and a SLO image. The main difference between fundus imaging and SLO is the mechanism by which they capture the image. SLO uses a laser to scan the retina point by point, creating a two-dimensional image with high resolution and contrast. Fundus imaging, on the other hand, captures a wider field of view and creates a two-dimensional image by taking a photograph of the fundus using a specialized camera.

2.4.2. Optical Coherence Tomography (OCT). OCT is an optical technique based on light interference that provides three-dimensional cross-sectional imaging of biological samples with a spatial resolution of 10 µm or less [**2**]. The underlying mechanism of OCT imaging is based on the principle of light interference. A schematic of an OCT system in the Michelson interferometer configuration is shown in Figure 2.4. The coupler splits the light from a low-coherence source into two arms of the interferometer, the reference arm and the sample arm. In OCT, the reference arm

(a) Fundus photograph of the retina [**39**]

(b) Image obtained by SLO

FIGURE 2.3. Comparison between fundus and SLO images

is actuated to enable precise control of the optical path length. A motorized translation stage or a piezoelectric actuator is commonly employed for the controlled movement of the reference mirror. By adjusting the position of the reference mirror, the optical path length of the reference arm can be modified, thereby changing the depth of focus or the position of the reference plane. As the light is backscattered from the reference mirror and the sample, it recombines at the coupler to create an interference pattern. This pattern is detected by a single point detector. The light in the reference arm of the OCT system is reflected by a reference mirror and returns to the interference system, propagating in the opposite direction but along the same path. The light in the sample arm also goes through the same process but is backscattered by the sample instead.

In OCT, A-scan refers to a one-dimensional image produced by measuring the reflection of light waves at a single point within a tissue. This provides information about the depth of a particular structure within the tissue being imaged. A B-scan is a two-dimensional cross-sectional image of the tissue being imaged. This provides a view of the tissue layers and structures within the tissue. Figure 2.5 shows a B-scan of a healthy retina showing the macular region.

There are 2 main classifications of OCT:

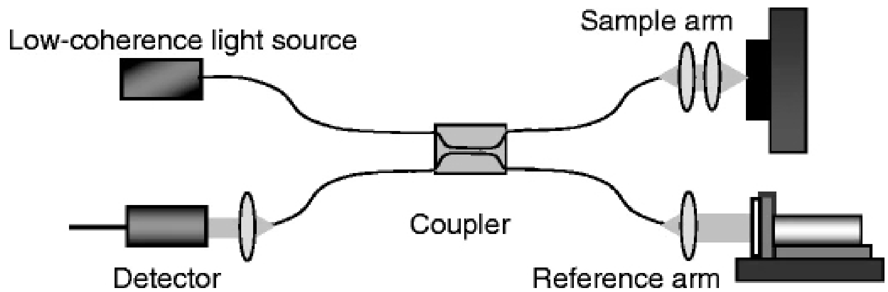

FIGURE 2.4. Principle of OCT [**2**]

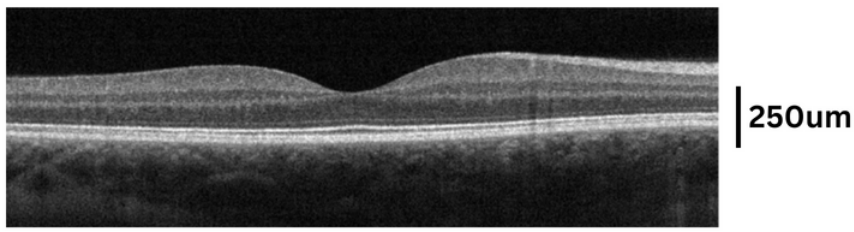

FIGURE 2.5. An OCT image (B-scan) of a healthy retina

- **Time Domain OCT:** Time domain OCT (TD-OCT) was the first generation of OCT and it measures the echoes from different depths in the sample by scanning a reference mirror in the reference arm. The axial resolution of TD-OCT is limited by the speed of the reference mirror, which restricts the imaging speed.
- **Fourier Domain OCT:** Fourier domain OCT (FD-OCT) is a type of spectral domain OCT that uses a spectrometer to capture interference patterns. In TD-OCT, light echoes are detected sequentially by the movement of a reference mirror, while in FD-OCT, the light echoes from all depths are detected at the same time, as the spectrometer splits the light into its different wavelengths and their spectral components are captured simultaneously. In an FD-OCT system, the reference arm has a static mirror, while in TD-OCT, a moving mirror is used. FD-OCT is further broadly classified into two types:
  - **Spectral Domain OCT:** Spectral domain OCT (SD-OCT) is a type of OCT that uses a spectrometer to analyze the interference pattern of light waves reflected from different depths within a tissue sample. In SD-OCT, the light echoes from different tissue layers are detected simultaneously, allowing for much faster acquisition speeds compared to TD-OCT.

- **Swept Source OCT:** Swept-source OCT (SS-OCT) is a type of OCT technology that employs a tunable laser as a light source. The laser output is swept across a range of frequencies, and the interference signal is detected as the laser sweeps.

The main difference between SD-OCT and SS-OCT is the type of light source and detection method used. In SD-OCT, a broadband light source is used, and the spectral interference pattern is measured with a spectrometer. In SS-OCT, a swept laser is used as the light source, and the interference signal is detected by a photodetector. SS-OCT has a faster scanning speed and longer imaging depth range due to the faster sweep rate of the laser, making it well-suited for imaging deeper structures such as the choroid. SD-OCT, on the other hand, has higher axial resolution and is better suited for imaging the superficial layers of the retina.

CHAPTER 3

Design

The conceptual design of the VR headset based multi-modal retinal imaging setup is shown in Figure 3.1. In this design, there are two components:

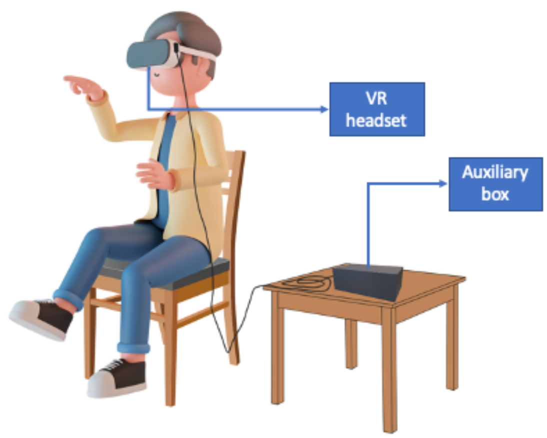

FIGURE 3.1. The conceptual setup of the VR headset based multi-modal retinal imaging

- **VR headset:** The VR headset includes a display screen and various optical components, such as lenses, mirrors, pupil tracking cameras, and actuators, which are responsible for directing the imaging light source towards the retina. An optical fiber and an electrical cable connect the VR headset to the auxiliary box.
- **Auxiliary box:** The controller and image acquisition modules, along with the light source, are situated in the auxiliary box, which is positioned near the user. To ensure the VR headset's comfort for the user, the auxiliary box contains components that could be regarded as too heavy for the headset to hold.

The VR headset and auxiliary box are connected by a lengthy cable that permits the user to move freely without the need for head stabilization. The separation of VR headset and auxiliary box enables multi-modal retinal imaging since OCT and SLO necessitate separate image acquisition modules and light sources. Housing these components in the auxiliary box allows for the optical components in the headset to be kept as is, while the OCT and SLO image acquisition can be performed parallelly in the auxiliary box.

The choice of optics within the headset depends on several factors, including the lateral resolution of OCT, the field of view of the retina, and space constraints. These factors determine the appropriate lenses, mirrors, and actuators to be used in the headset.

3.1. 4f optical system

A 4f optical system is an optical setup consisting of two lenses separated by a distance equal to the sum of their focal lengths. The first lens takes an object and produces an intermediate image that is further magnified by the second lens, forming a final image at the output. The name "4f" comes from the fact that the distance between the input and output planes of the system is equal to four times the focal length of each lens. In this design, as shown in figure 3.2, because the lenses are identical, the distance between the two lenses is 2f, while the distance between the object plane and lens #1 and the distance between lens #2 and the image plane are both equal to f.

In essence, the 4f system ensures that a parallel beam of light at the object plane remains parallel at the image plane, while a diverging light source at the object plane is focused into a point at the image plane. An important aspect of this design is that the focusing of the light ray onto the retina is reliant on the eye's refractive properties. A collimated laser source at the object plane results in a collimated beam at the image plane, which allows for the human eye to focus the light onto a point on the retina as shown in figure 3.2. As eye accommodation is not required for performing spectral domain OCT, the optical design is independent of the patient's accommodative requirements.

Moreover, for imaging different areas of the retina, the collimated laser source goes through raster scanning. This results in the light converging from various angles at a focal point on the

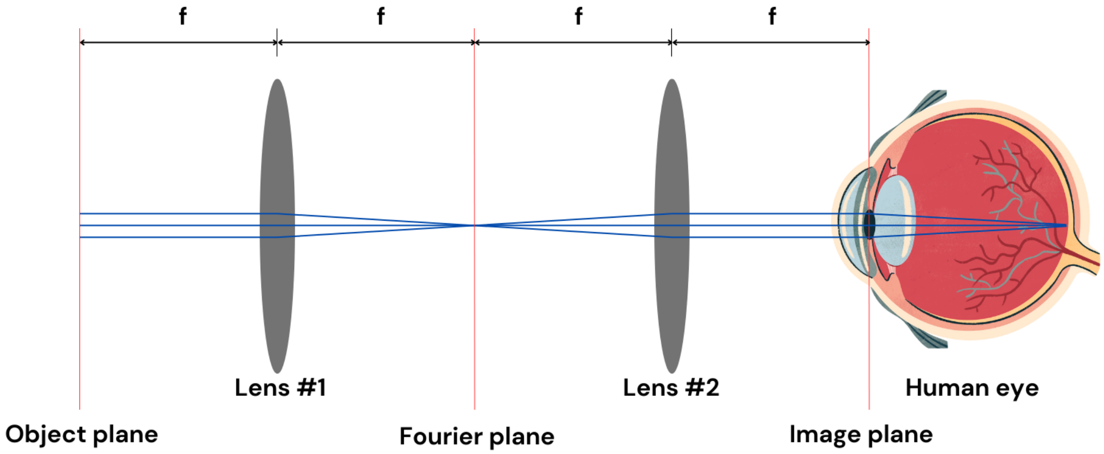

FIGURE 3.2. A collimated beam or laser at the object plane will produce a collimated beam at the image plane, which will be focused onto a point on the retina due to the refractive properties of the layers of the eye.

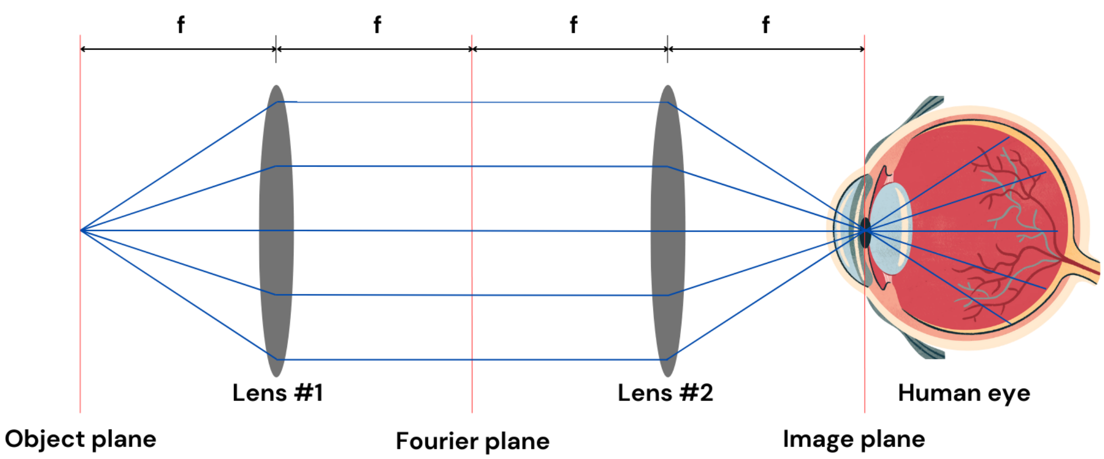

FIGURE 3.3. The collimated beam of light can be incident onto lens #1 at multiple angles and can pass through the pupil of the eye kept at the image plane thereby generating a wide FOV image of the retina. Each light ray in the figure represents a collimated beam of light similar to figure 3.2

image plane before being projected onto different points on the retina as shown in figure 3.3. To achieve this, the pupil of the eye should be at the image plane.

3.2. Optical Actuation

3.2.1. Raster scanning. Raster scanning is a technique used in imaging where a scanning device, such as a laser beam or electron beam, moves back and forth across an object or surface in a series of parallel lines, creating a grid or raster of pixels. Figure 3.4 demonstrates the sweeping pattern of a raster scan. The electron beam in the figure represents the collimated beam focused onto the retinal surface in the case of OCT, and the generation of OCT B-scans is achieved through the process of raster scanning.

In order to raster scan the light from the laser source, actuation is required. Galvanometer-based optical scanner (Saturn 1B, ScannerMax), which utilizes a motor-driven physical mirror to enable scanning functionality was chosen for actuation as its step response is fast enough to perform an OCT scan. In the design, the galvanometer is placed at the object plane.

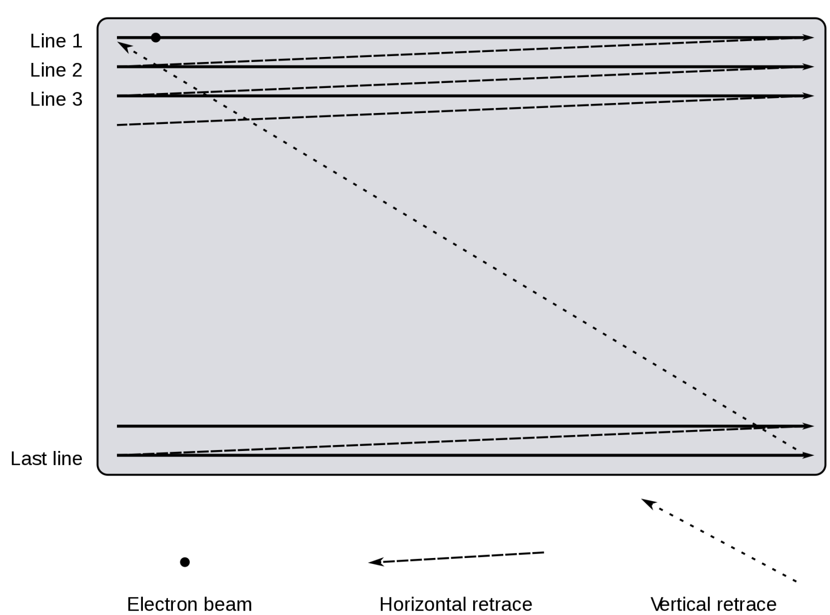

FIGURE 3.4. Sweeping pattern of a raster scan

3.2.2. Pupil Tracking. While mechanical head stabilization is not required as the optics moves with the patient, pupil tracking is required. Since the only aperture for the light to enter the eye and image the retina is the pupil, the movement of the pupil away from the optical axis would result in the light hitting the surface of the eye or cornea and not imaging the retina. Thus, it is important to track the pupil movement and re-direct the light through the axis normal to the pupil.

The system to perform pupil tracking and optical correction involves two things:

- **Pupil tracking camera:** To track the pupil movement in real time, pupil cameras from Pupil Labs were chosen. The pupil cameras determine the center coordinates and size of the pupil on a 2D coordinate system in pixels, as well as on a 3D coordinate system using a prediction model.
- **Actuation:** Based on the real time location of the pupil in the 3D global coordinate system as obtained from the pupil camera, fast steering mirror (FSM) (OIM202.3, Optics in Motion) was chosen to steer the light into the axis normal to the pupil thereby ensuring that the light always passes through the pupil and hits the back of the eye.

Optical axis correction based on pupil position has the advantage of enabling a wider field of view of the retina, as directing light to the retina from different angles would provide greater retinal coverage. A broader field of view can be attained in a managed approach by leading the patient's gaze towards various sections of the VR headset screen. This can be accomplished by playing videos that attract the patient's attention to different parts of the screen.

3.3. Choice of lens

In this design, the choice of lens based on parameters such as focal length, diameter and thickness becomes paramount. There are two main considerations to keep in mind while choosing the lenses:

- **Space constraints:** The limited space inside the VR headset necessitates the accommodation of all the optical components, such as lenses, FSM, and galvanometer, along with other mirrors. The amount of space occupied by the lens increases with its thickness, reducing the space for other optical components. Although a higher focal length provides more distance between the two lenses and hence more space, we must also ensure that all the components can fit into the mechanical constraints of the headset.

- **Field of view:** As the focal length of the lenses increase, the distance between lens #2 and the eye increases. As this distance increases, the field of view of the retina reduces. The smaller the focal length, better the field of view.

Thus, the choice of lenses is a trade-off between space limitations and achievable field of view. Fresnel lenses (FRP251 - Ø2”, ThorLabs), with a focal length of 51 mm and a diameter of 2 inches was chosen for this project. The diameter of these lenses is similar to that of a standard VR headset lens, while the 1.5 mm thickness takes up minimal space, allowing for additional components in the headset.

3.4. Headset design

The schematic of the optics used in the VR headset is presented in Figure 3.5, which considers various factors and design considerations discussed earlier. The design presented here builds upon the contactless robot-mounted OCT scanner research by utilizing the same optical actuators and a 4f optical system described in [**24**], but with a different lens.

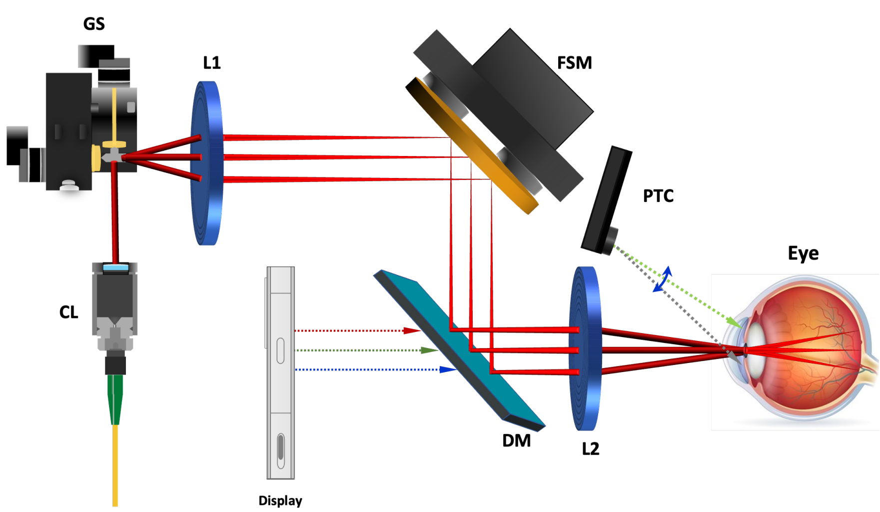

FIGURE 3.5. Schematic of the headset design. DM: Dichroic mirror; FSM: Fast Steering Mirror (XY scan); PTC: Pupil Tracking Camera; L1 & L2: Relay and Objective lenses; GS: Galvo Scanner (Dual axis); CL: Collimating lens

The optical pathway of the laser begins with the laser source and the collimating lens. The light is reflected by the galvanometer or galvo scanner to lens #1 or the relay lens in a raster scanning pattern. The FSM redirects the light to ensure that it enters the eye via the axis perpendicular to the pupil, based on the output from the pupil tracking camera. In this design, a dichroic mirror is utilized that reflects light of specific wavelengths while allowing others to pass through, reflecting the laser with a center wavelength of 1,060 nm and transmitting visible spectrum light. This feature enables the user to view the video on the VR display, while the light source for imaging follows the same optical pathway. The light from the dichroic mirror is directed to the eye from lens #2 or the objective lens. The placement of lenses, eye and the galvanometer follow the 4f optics system as described in figure 3.2 and figure 3.3.

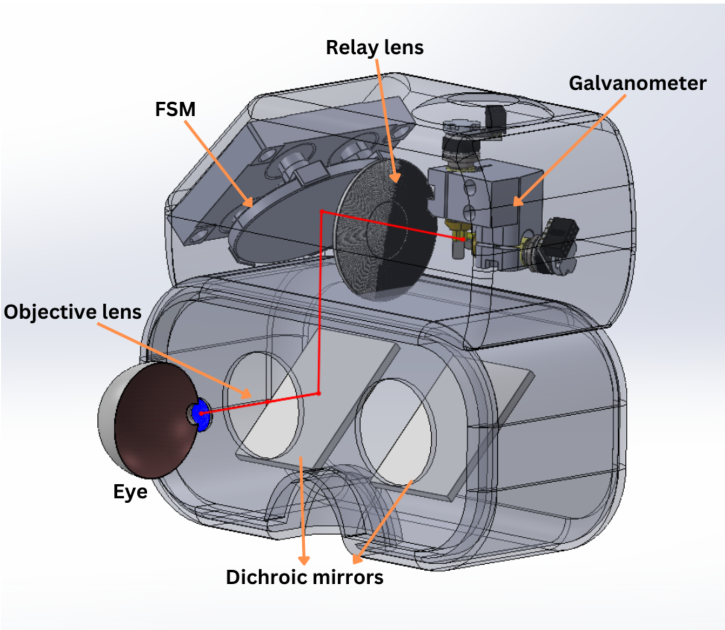

FIGURE 3.6. The arrangement of the optical components inside the prototype headset enables imaging of one eye at a time. The top compartment, that houses galvanometer, relay lens and the FSM can be flipped as shown in figure 3.7 to image the other eye.

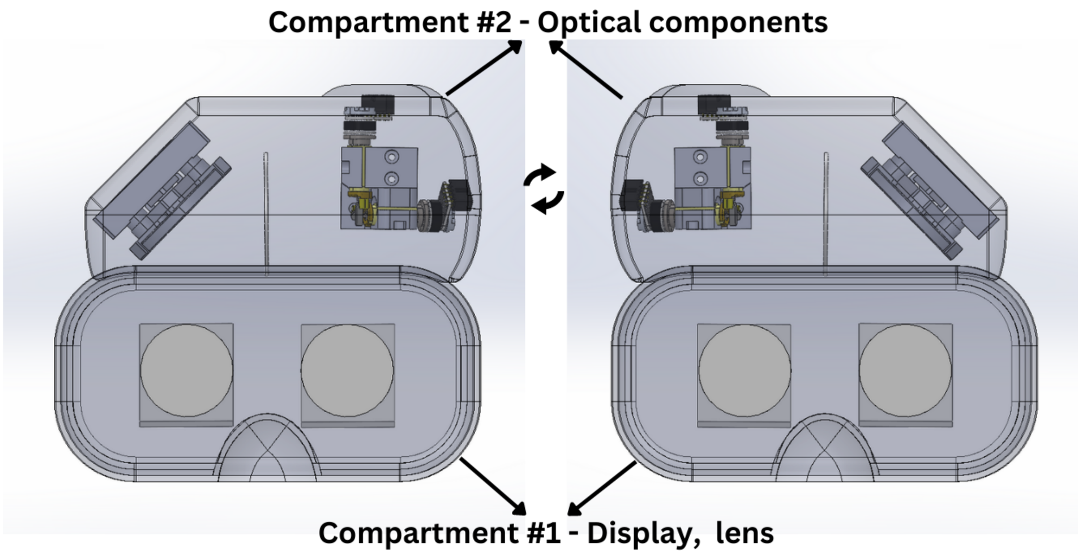

FIGURE 3.7. The front view of the headset, containing two compartments. The bottom compartment contains the lens, dichroic mirror and the display screen, while the top compartment houses the galvanometer, FSM and relay lens and is detachable. It can be flipped as illustrated to enable imaging of the other eye. The left figure displays the arrangement for imaging the left eye of the patient, while the right figure displays the arrangement for imaging the right eye of the patient.

The design of a prototype headset that incorporates the optical components is shown in figure 3.6. In this prototype, the optical components are housed in a compartment that can be attached on top of a typical VR headset. The space between these two compartments is optically transparent in order to allow for light to pass through. With the prototype design, we can image one eye at a time. Once, one eye is imaged, the top compartment can be removed, rotated and slotted back into place in the opposite direction, which would allow for the other eye to be imaged. The mechanism for rotating the top compartment is shown in figure 3.7. The estimated weight of the headset is 650 to 750 grams, which falls within the weight range of the commercially available VR headsets.

3.5. Optical simulations

To validate the feasibility and optical performance of the preliminary design, OpticStudio simulation software was used. The tool was used to validate the field of view of the system, spot size along with optimizing the optical system. Figure 3.8 depicts the arrangement of various optical components, which were modelled on OpticStudio. The dimensions of all the modelled optical components are according to the commercially available components as described below.

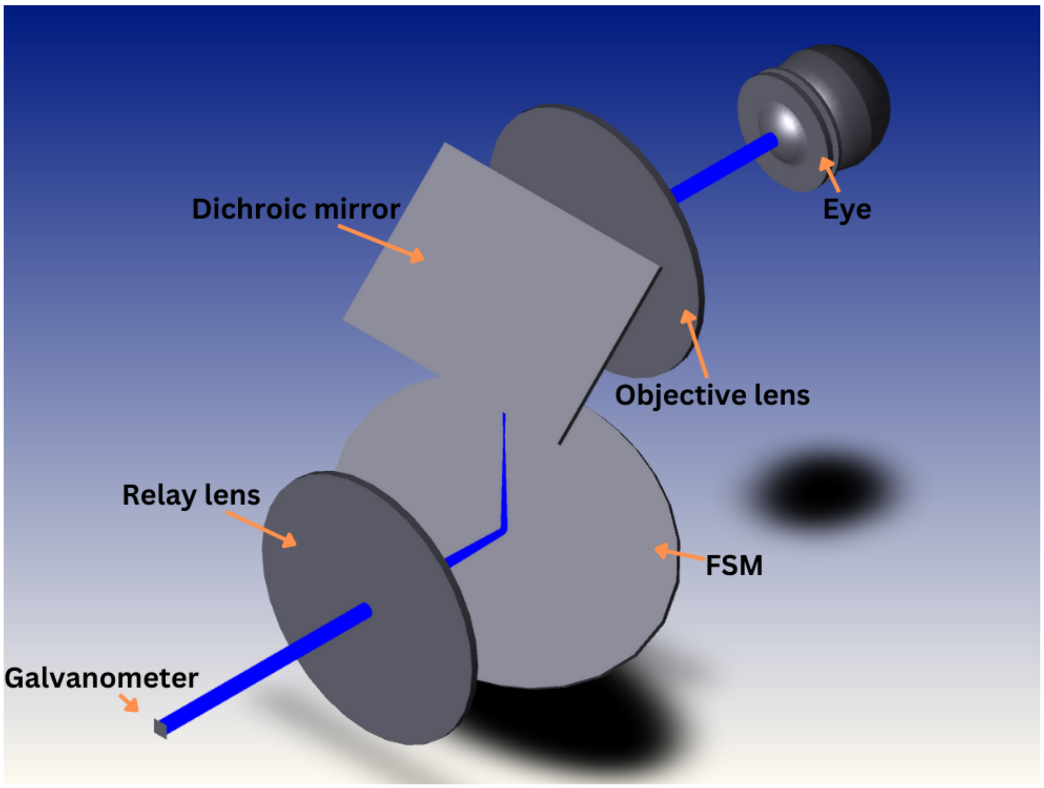

FIGURE 3.8. The placement of the optical components and light path can be observed in the 3D model created in OpticStudio. The galvanometer, FSM, and dichroic mirror are represented as mirrors, with the first two having the ability to rotate about the x and y axes.

The optical components used in the design include relay and objective lenses in the form of Fresnel lenses (FRP251 - Ø2", ThorLabs), with a diameter of 2 inches and a focal length of 51 mm. The model files of the Fresnel lenses from ThorLabs were imported into OpticStudio. The galvanometer was modeled with a circular aperture of radius 3 mm. For the simulation of the galvanometer's movement, its maximum rotation range of ±27.5°was taken into consideration. The

FSM, which was modeled as an elliptical mirror with dimensions of 2.1 x 3.0 inches according to the selected OIM202.3 Optics in Motion FSM, has a rotation range of ±3°. The dichroic mirror was modeled as a 35 mm x 52 mm rectangular mirror as per the DMBP740B dichroic mirror from Thorlabs. The eye model used was imported from the sequential eye model developed by OpticStudio. All the simulations were performed with the wavelength of light being 1,060 nm, which is the center wavelength of the chosen laser source.

The 4f optical system is utilized to maintain specific distances between the optical components, with 'f' being 51 mm(FRP251, ThorLabs). Although it would have been ideal to place the FSM at the Fourier plane, our observation suggests that its placement between the relay lens and the objective lens does not compromise the system's performance. As the optical performance was unaffected by the FSM placement, the FSM was placed slighly before the Fourier plane, a decision taken to address the mechanical placement constraints within the VR headset shown.

3.5.1. Field of view (FOV). The system's field of view was determined by creating a grid of raster scan pattern through the rotation of the galvanometer along its x and y axes. Due to the dimensions of the FSM and dichroic mirror and orientation of the optical components, a raster scan grid generates a FOV grid that is rectangular and not square, with limitations along the y-axis.

3.5.1.1. ***Centered FOV.*** According to the simulation, moving the galvanometer horizontally by an angular range of ±20.5°and vertically by an angular range of ±12°allows for achieving the maximum field of view of the retina without any aberrations when the eye is centered and normal to the optical axis. Figure 3.9 shows the 3x3 raster scan grid generated by the galvanometer and the path of light through the optical system due to the various angular configurations of the galvanometer.

In this simulation, 9 angular configurations of the galvanometer have been considered to generate a 3x3 raster scan grid. Each one of these angular configurations, targets a point on the retina. These angular configurations have been chosen to create a boundary to demonstrate the area of the retina that can be imaged. The relationship between the field of view of the retina and the angular configuration of the galvanometer is illustrated in Table 3.1. The x-axis and y-axis angles that the retinal incident spot forms with the optical axis, as measured from the cornea of the eye, are represented by FOV x and FOV y, respectively, in the table. Figure 3.10 illustrates the spots formed

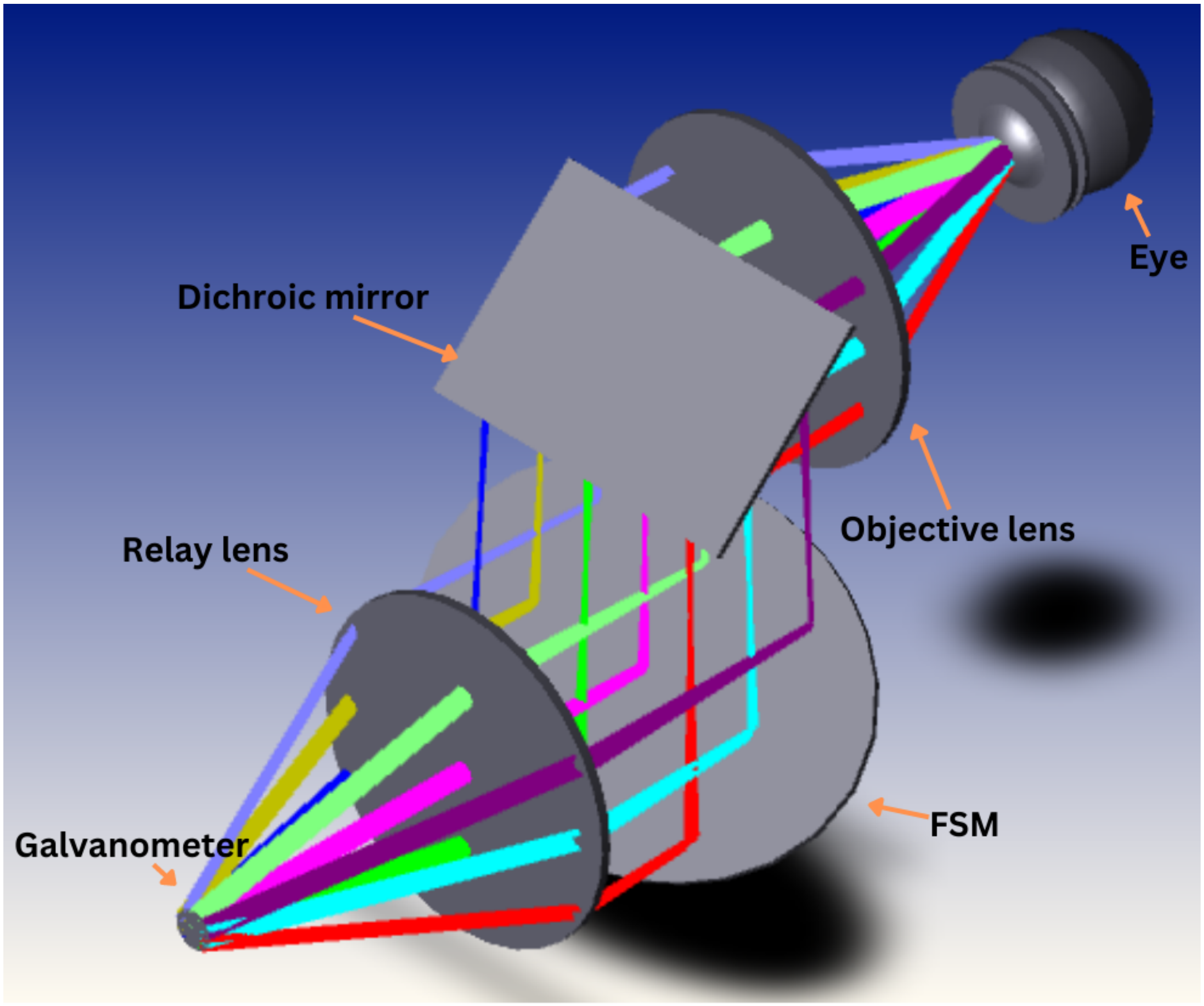

FIGURE 3.9. The grid raster scan pattern (3x3 grid) generated from the movement of the galvanometer about its x and y axes when the eye is centered and normal to the optical axis. Each color in the figure represents the light path from a different angular configuration of the galvanometer. In this figure, the galvanometer moves with a horizontal angular range of ±20.5°and a vertical angular range of ±12°

on the retinal surface from the galvanometer raster scan. Figure 3.11 shows the spot diagram for every angular configuration of the galvanometer on the retinal surface. A horizontal retinal FOV of ±15°and a vertical retinal FOV of ±9°is achieved as measured from the cornea which corresponds to an area of approximately 80 mm^2 (11.148 mm horizontal and 6.944 mm vertical) on the retina.

3.5.1.2. ***Off-center FOV***. By controlling the patient's gaze during the test, the FOV of the eye that can be imaged can be increased beyond the ±15°horizontal and ±9°vertical FOV achieved

TABLE 3.1. Galvanometer configuration and corresponding FOV angles

Configuration	Galvo x	Galvo y	FOV x	FOV y
1	20.5°	-12°	-15°	9°
2	0°	-12°	0°	9°
3	-20.5°	-12°	15°	9°
4	20.5°	0°	-15°	0°
5	0°	0°	0°	0°
6	-20.5°	0°	15°	0°
7	20.5°	12°	-15°	-9°
8	0	12°	0°	-9°
9	-20.5°	12°	15°	-9°

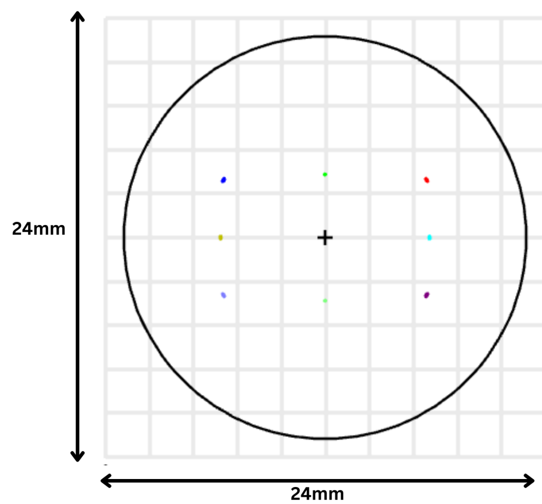

FIGURE 3.10. The footprint diagram illustrates the spots formed on the retinal surface as a result of the galvanometer raster scan. Since the eye is represented as a sphere having a diameter of 22 mm, the retinal surface is depicted as a circle with the same diameter. The colors of the spots indicate the light emitted from 9 different angular configurations of the galvanometer. These colors correspond to the light beam configuration shown in Figure 3.9.

when the eye is centered along the optical axis, as demonstrated in the previous section. While the typical ranges of eye movement are 44.9 ±7.2°in adduction, 44.2 ±6.8°in abduction, 27.9 ±7.6°in elevation, and 47.1 ±8.0°in depression [**40**], the controllable eye gaze angles in this project are determined by the headset design and the screen dimensions.

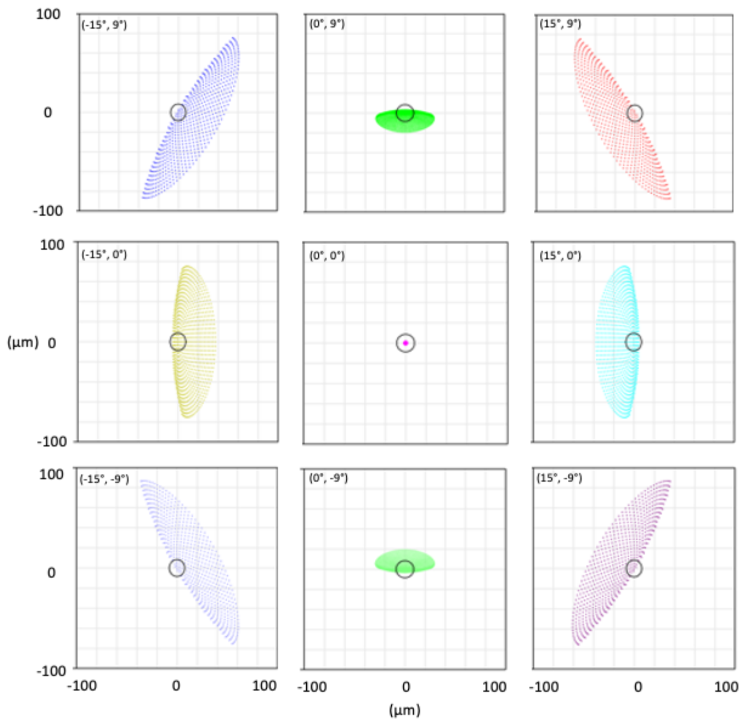

FIGURE 3.11. The spot diagram shows the spot size formed at every angular configuration on the retinal surface. These colors correspond to the light beam configuration shown in Figure 3.9 and Figure 3.10.

The gaze angle of the eye that can still see the corners of the screen is approximately $\pm 27°$from the optical axis, as illustrated in Figure 3.12. Since the light from the screen is collimated, the angle the eye makes with the edges of the lens determines the maximum gaze angle. By carefully selecting the video content displayed on the screen, the user's gaze can be directed to different regions of the screen, providing a $\pm 27°$range of flexibility in gaze movement. Figure 3.13 shows the different gaze angle configurations of the eye in the simulation. The eye is tilted by $\pm 27°$along its x and y axes to obtain 9 configurations where the eye is gazing at the corners of the screen along with other configurations as seen in figure 3.13. To ensure that all the light enters through the pupil, the FSM is rotated about its x and y axes, since the pupil location and aperture size as viewed from the optical axis change for each gaze angle. To ensure that light enters the pupil without aberrations, the FSM would need to tilt at most ±0.75°for a gaze angle of ±27°from the optical axis. With the maximum tilt angle of the OIM202.3 Optics in Motion FSM being ±3°, ±0.75°falls well within the angular range of the actuator.

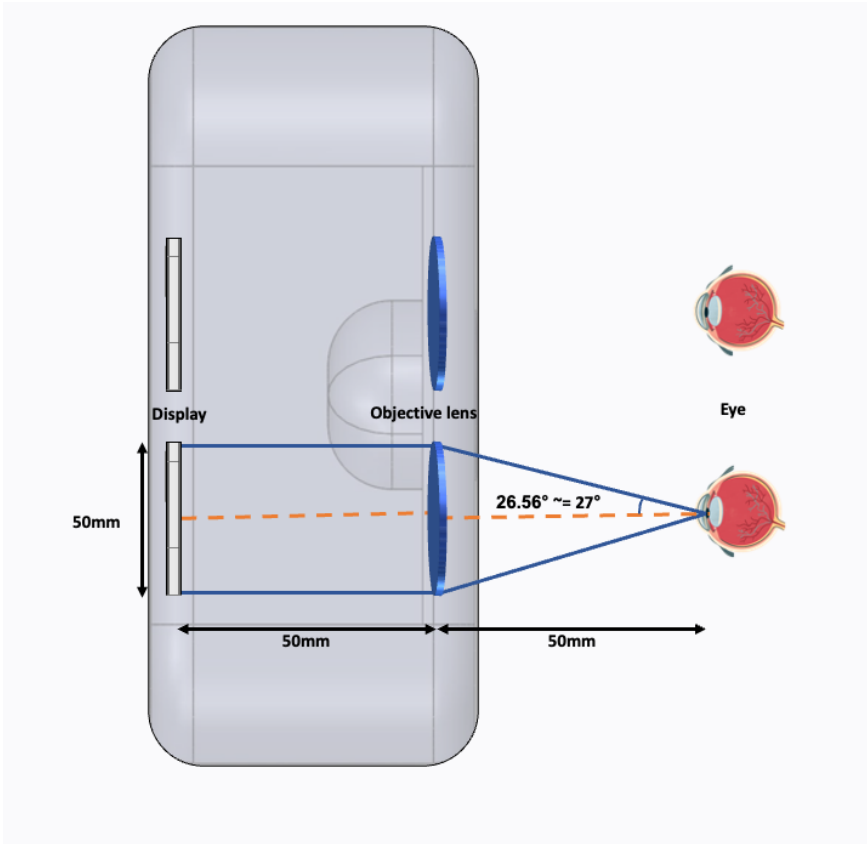

FIGURE 3.12. The combination of the headset design and screen dimensions enables the eye to reach the border of the screen with a 27-degree gaze angle from the optical axis.

Figure 3.14 shows the field of view coverage on the retina for each of the 9 gaze angle configurations of the eye. Each image in Figure 3.14 corresponds to the area of the retina imaged corresponding to a specific gaze configuration angle, as demonstrated in Figure 3.13.

By combining the area of coverage of the retina as shown in figure 3.14, for all gaze angle configurations, figure 3.15 can be obtained which shows the maximum area of the retina that is covered by the laser provided that the gaze angle of the eye is controlled. This results in the wide-field FOV of the system being expanded to ±25°horizontally and ±23°vertically as measured from the cornea, by considering the various off-center gaze angles of the eye. By leveraging these

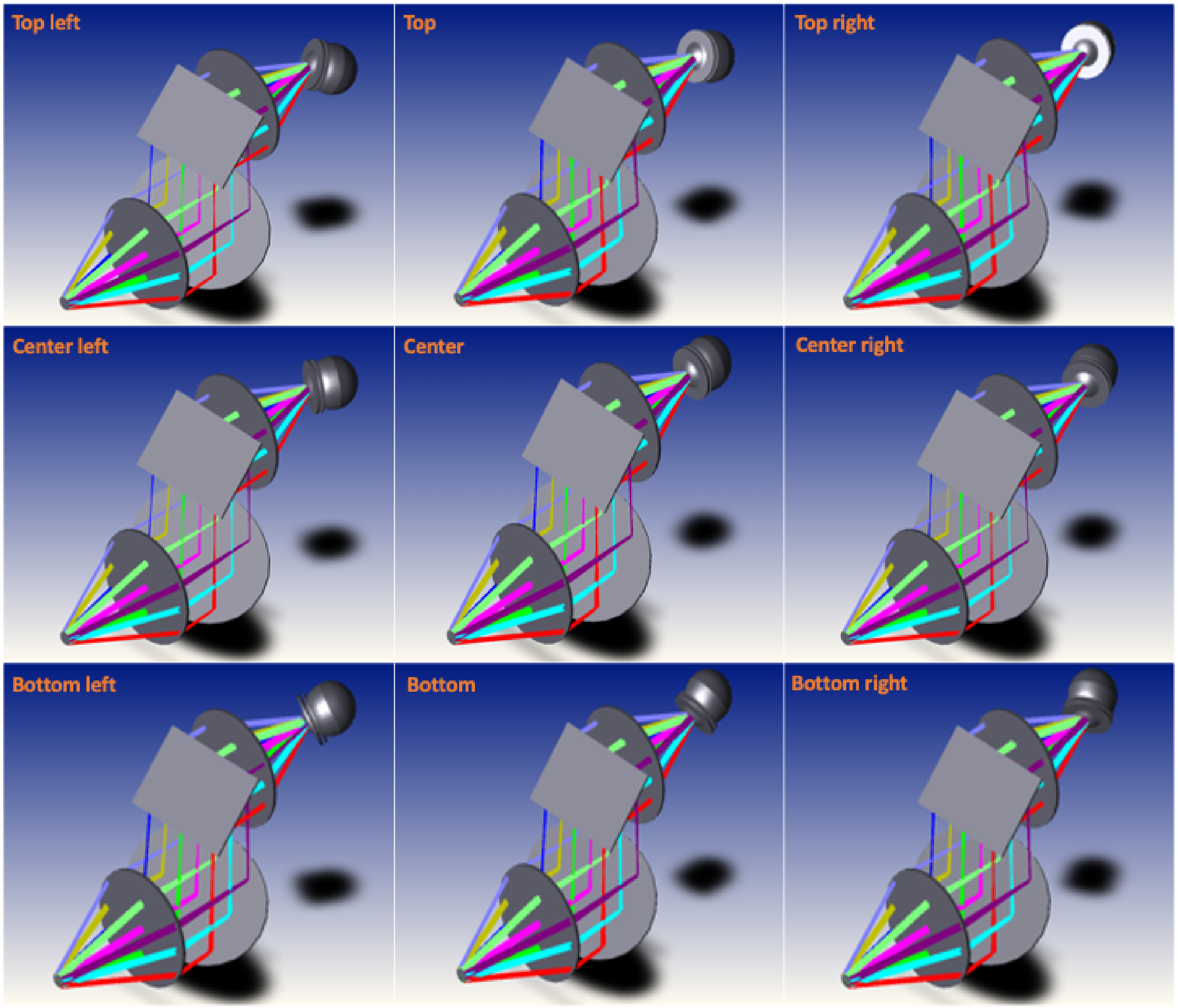

FIGURE 3.13. Different gaze angles of the eye that can view the edges of the display screen. The gaze angles of the eye are obtained by moving the eye ±27°along x and y axes. The top-left subfigure depicts the eye looking towards the top-left from the observer's point of view, while the bottom-right subfigure depicts the eye looking towards the bottom-right, and so on.

gaze angles, a +10°increase in horizontal FOV and a +14°increase in vertical FOV can be achieved when compared to the FOV of the system with a centered eye gaze. This covers an area of about 390 mm^2 on the retinal surface, with a maximum horizontal span of 20.76 mm and a maximum vertical span of 18.84 mm, which is almost 5 times larger than the field of view from the centered gaze.

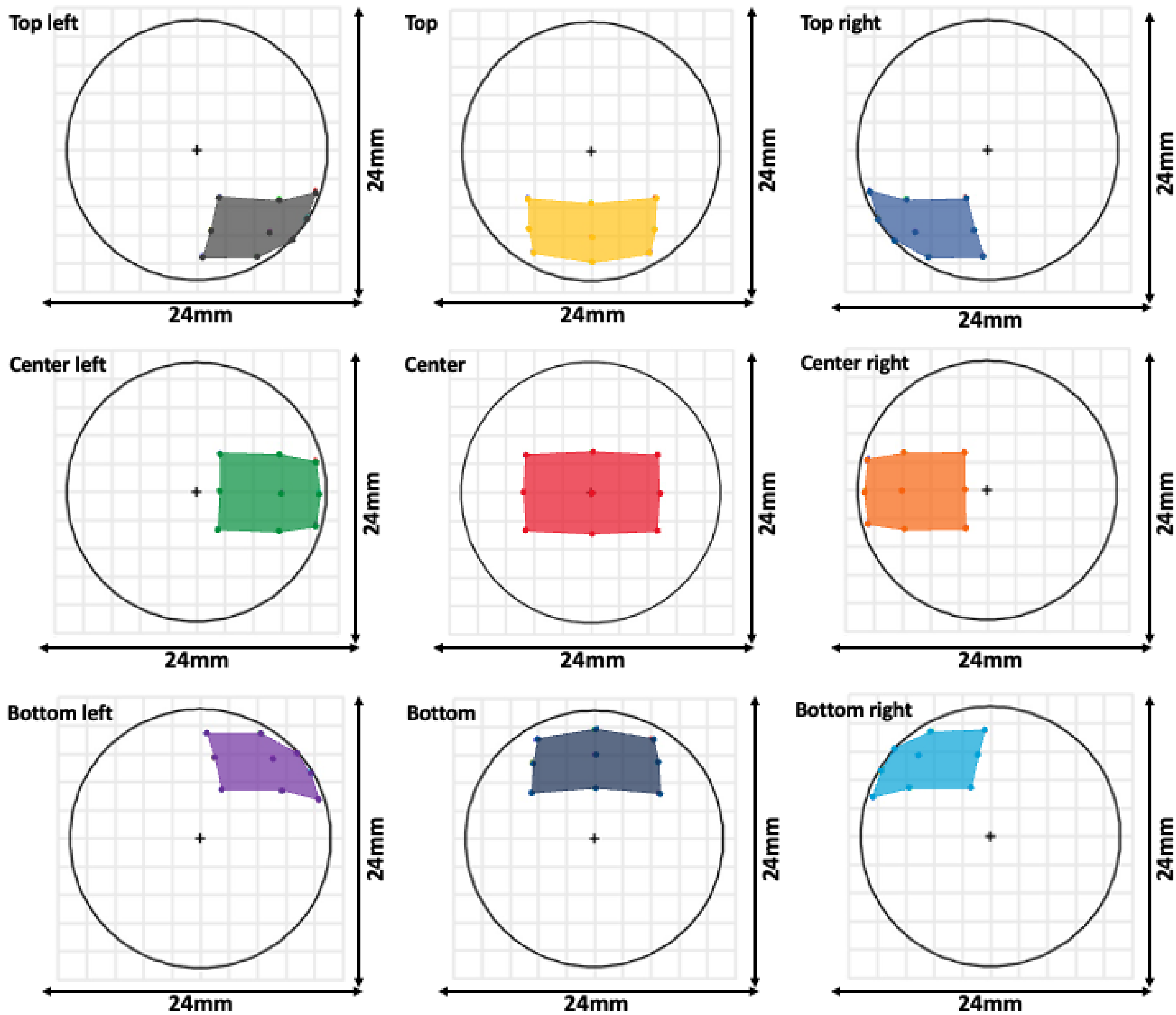

FIGURE 3.14. Field of view or the area of the retina covered by the optical system at different gaze angle configurations of the eye as shown in Figure 3.13.

3.5.2. Spot size. The simulation results reveal that the light beam along the optical axis achieves a diffraction-limited spot size, as demonstrated in the figure 3.16. With an entrance beam diameter of 2.5 mm, the Airy radius measures 8.725 µm. However, the spot size becomes larger as we move away from the optical axis, resulting in a non-diffraction-limited performance. Figure 3.11 shows that the spot size that exceeds the Airy disk as we move away from the centered beam. Although the spot size remains relatively small, it is not diffraction-limited at these angles. It was observed that the non-diffraction limited spot on the retina, which was contrary to the expectation

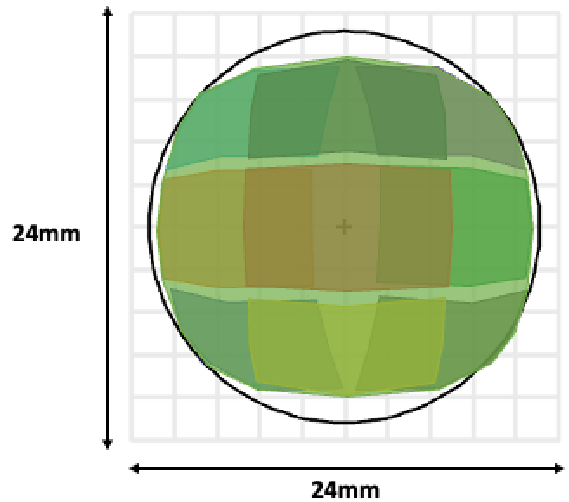

FIGURE 3.15. The combined area of coverage on the retina, obtained by combining the retinal coverage from all the different gaze angle configurations of the eye.

that a model eye should focus light at a point on the retina regardless of the incident angle, may be attributed to the imported eye model from Zemax OpticStudio [**41**]. To address this limitation, a model eye simulated on OpticStudio based on the widely-used Navarro eye design [**42**] could be developed in the future, which is beyond the scope of this thesis.

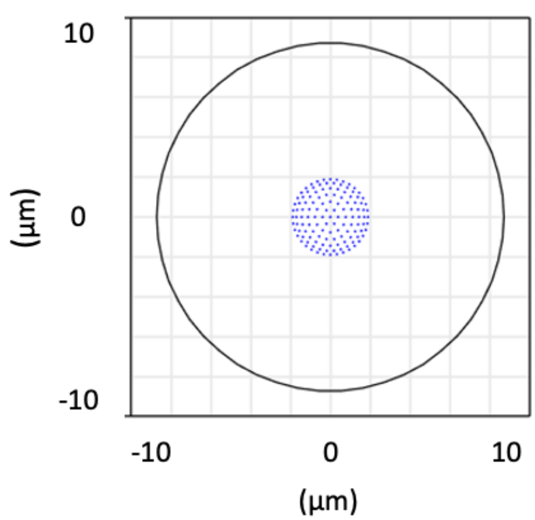

FIGURE 3.16. Spot diagram for the light beam travelling along the optical axis. The black circle shows the Airy disk with the radius of 8.725µm.

3.5.3. Discussion. The significance of the optical simulation results can be understood by analyzing the different areas of the retina that can be imaged. The structure and dimensions of the macula, fovea, and optic disc are shown in Figure 3.17. Figure 3.18 is obtained by overlaying the wide-field footprint diagram shown in Figure 3.15 with Figure 3.17. It can be observed that the significant regions of the retina crucial for diagnosis are covered by the raster scan and the combined footprint diagram, and that the field of view exceeds them.

In comparison with the results of the contactless robot-mounted OCT scanner paper, our findings demonstrate a wider field of view, measuring 50°x 46°, surpassing their achievement of 16°x 16° [**24**].

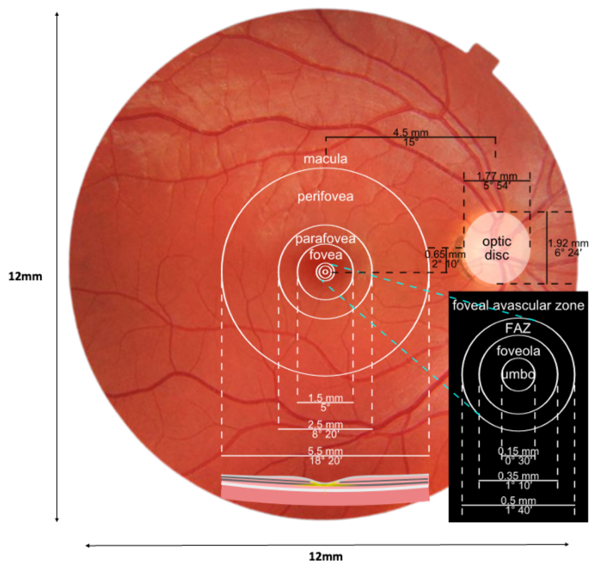

FIGURE 3.17. Photograph of the retina of the human eye, with overlay diagrams showing the positions and sizes of the macula, fovea, and optic disc. The structure and the dimensions of these regions are shown.

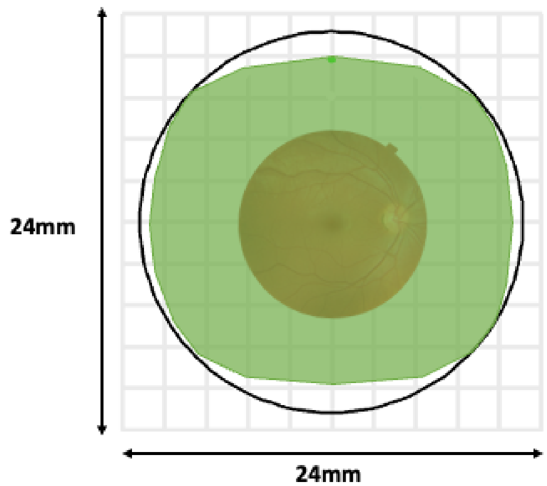

FIGURE 3.18. The combined footprint diagram obtained from the wide-field FOV optical simulation for all gaze angle configurations is overlaid on the photograph of the retina from figure 3.17 showing the macula region and the optic disc. The system's coverage area is capable of capturing the macula region, optic disc, surrounding blood vessels, and more.

CHAPTER 4

Pupil Tracking Experiments

To examine the characteristics of pupil movement, this study integrated pupil tracking cameras into a VR headset and presented a customized video to a group of four participants consisting of three adults and a 3-year-old toddler. The primary aim of the experiment was to investigate the influence of video selection on pupil movement and to determine if there were periods of time during which the pupil remained sufficiently stationary to enable the acquisition of OCT images.

4.1. Experiment design

The pupil tracking camera purchased from PupilLabs is originally designed to be used as an attachment to HTC Vive VR headset as shown in Figure 4.1.

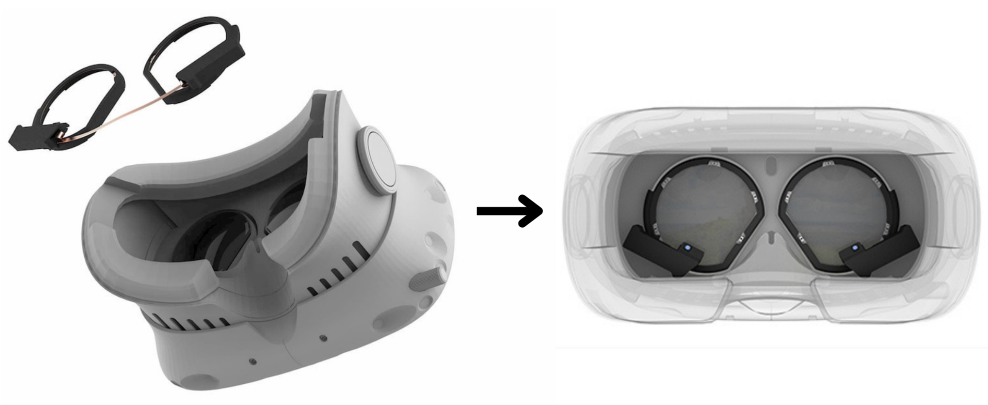

FIGURE 4.1. The pupil tracking camera from Pupil Labs designed to be attached to a HTC Vive VR headset.

A phone-based VR headset was utilized in our experiments, which employs a slide-in mechanism for using the smartphone as the screen. This headset was chosen in order to develop an inexpensive prototype for conducting the pupil tracking experiments. Figure 4.2 shows the development of the prototype VR headset used for the experiments.

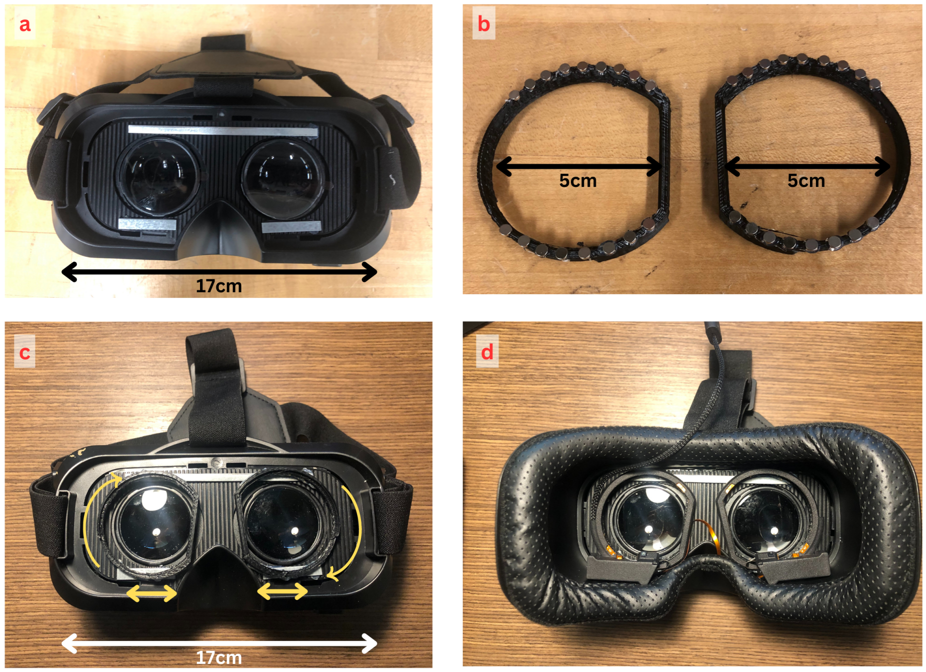

Figure 4.2. The fitting and design of the headset used for conducting pupil tracking experiments are shown in figures 1-4. Subfigure (a) displays metal strips attached to the front of the headset's face to enable linear and rotational movement of the pupil cameras attached with magnets. Subfigure (b) shows 3D printed camera mounts with attached button magnets, which are secured to the metal strips on the headset as depicted in subfigure (c). This setup allows for camera movement and adjustment to ensure that the pupils remain in frame. Finally, subfigure (d) shows the VR headset with the attached pupil cameras and face rest.

For the experiment, a video consisting of three smaller videos was curated. The first video was sourced from the popular YouTube series called Simon's Cat, chosen for its predominant static nature and minimal movement, with the only animation being that of the cat character. The duration of this video was 1 minute 30 seconds. The second video presented a stationary red ball in the center of the screen for 15 seconds, serving as a reference video to determine the amount of gaze movement relative to other videos. The third video featured the same red ball moving to the corners of the screen, intended to confirm that the displayed video could control the viewer's gaze.

4.2. Results

The pupil labs API provides 2D as well as 3D pupil detection. The 2D pupil detection method aims to locate a 2D ellipse that fits the pupil in a given eye image. On the other hand, the 3D pupil detection method utilizes a mathematical 3D eye model to capture ocular kinematics and optics. Both detection methods yield a confidence score ranging from 0 to 1, where 0 indicates a failure to detect the pupil, and 1 denotes a high degree of certainty in the detection. For this experiment, 2D pupil detection was employed to determine gaze angles and duration, as 3D pupil detection requires calibration to achieve a good confidence score, and participants were not instructed to undergo calibration. Pupil data having a confidence score of 0.8 and higher were selected for analysis.

Figure 4.3 demonstrate that distinct intervals of stationary pupil can be isolated while the user is watching the Simon's cat video. The Simon's cat video was observed by a toddler and an 80 second interval of the recorded toddler's pupil position is presented in the figure. The normalized pixel position is defined as the normalized 2D image space with the origin (0,0) at the bottom left corner and the top right corner at (1,1). Distinct intervals of stationary pupil for as long as 6 seconds are depicted in the close-up view (Fig. 4.3, insert (a)), which was obtained from the toddler's pupil tracking data. These stationary intervals coincide with the frames in the video where the cat remains relatively still, as shown. These stationary intervals are consistent across all recordings of the experiment participants. Insert (b) of Figure 4.3 is presented to benchmark the stationary pupil intervals and it shows the pupil position of an adult while staring at the static red ball in the middle of the screen.

TABLE 4.1. Variances of the normalized pixel position of the pupil during different videos

Video	Right Eye		Left Eye	
	Variance x	Variance y	Variance x	Variance y
Simon's cat	1.1 x 10^{-4}	1.5 x 10^{-3}	7.8 x 10^{-5}	2.5 x 10^{-3}
Stationary red ball	5.6 x 10^{-5}	9.7 x 10^{-5}	1.3 x 10^{-4}	1.7 x 10^{-4}

The variances of the normalized pixel positions of the toddler's pupil as displayed in insert (a) of figure 4.3 while watching the Simon's cat video and the normalized pixel pupil position of the adult as displayed in insert (b) while watching the centered static red ball of the same figure are compared in Table 4.1. It is noted that the pupil position variations when the adult stares at a red ball were of similar magnitude to those of the isolated pupil intervals observed in the toddler measurements acquired while watching an animation. This provides evidence that discrete intervals for capturing OCT images can be obtained while the user watches a video.

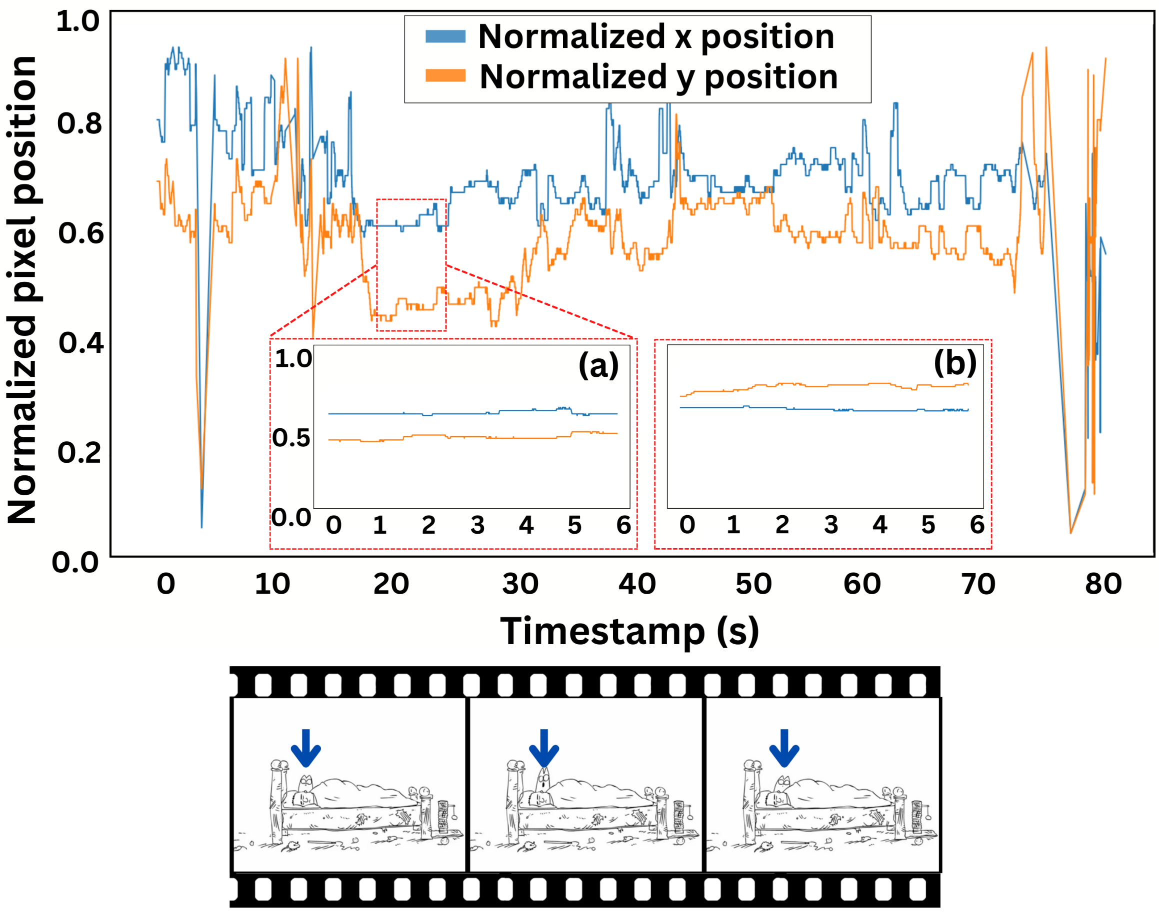

FIGURE 4.3. Pupil position vs. time acquired while a toddler watched an animation. The measurement features isolated episodes of stationary pupil (insert a). An example 6 sec interval of pupil movement measurement acquired when an adult is asked to stare at a stationary small circle on the headset screen is included for comparison (insert b).

To determine the influence of the video on the user's gaze, a video was presented to the participants, where a red ball sequentially moves from the center of the screen to each of the four corners, remaining stationary for 5 seconds at each position. The normalized pupil positions during the 40s video, depicting the movement of the red ball to various points, are displayed in Figure 4.4. The correspondence between the changes in the pixel positions and the video frames is depicted using red dotted lines. The movement of the ball to different corners of the screen results in corresponding movements in the pupil positions, illustrating that the correct video can be chosen to manipulate the participant's gaze. It was observed that the instructions to follow the red ball on screen were better followed by adults than the toddler. Additionally, it was noted that the animated video was more interesting to the toddler than the red ball. Hence, choosing a suitable video is crucial, as it must not only direct the person's gaze but also be captivating for individuals with mental or intellectual disabilities and toddlers.

4.3. Discussion

Our initial findings suggest a couple of things: first, that selecting the appropriate video for the user can isolate discrete intervals of time with limited pupil movement that are adequate for acquiring an OCT image, and second, that the user's gaze can be controlled. This is significant as controlling the gaze enables the capture of a wider field of view of the retina, enhancing the effectiveness of the optics.

The pupil camera is capable of capturing images at a rate of 120 frames per second, which aligns with the response characteristics of the Fast Steering Mirror described in Chapter 3. The pixel positions obtained from the pupil camera serve as input to a control algorithm that regulates the movement of the FSM, ensuring that the light enters the eye at an axis normal to the pupil. This control mechanism not only facilitates the imaging of a wider angle of the retina but also assists with retinal image registration using the ground truth of the pupil position and FSM angle.

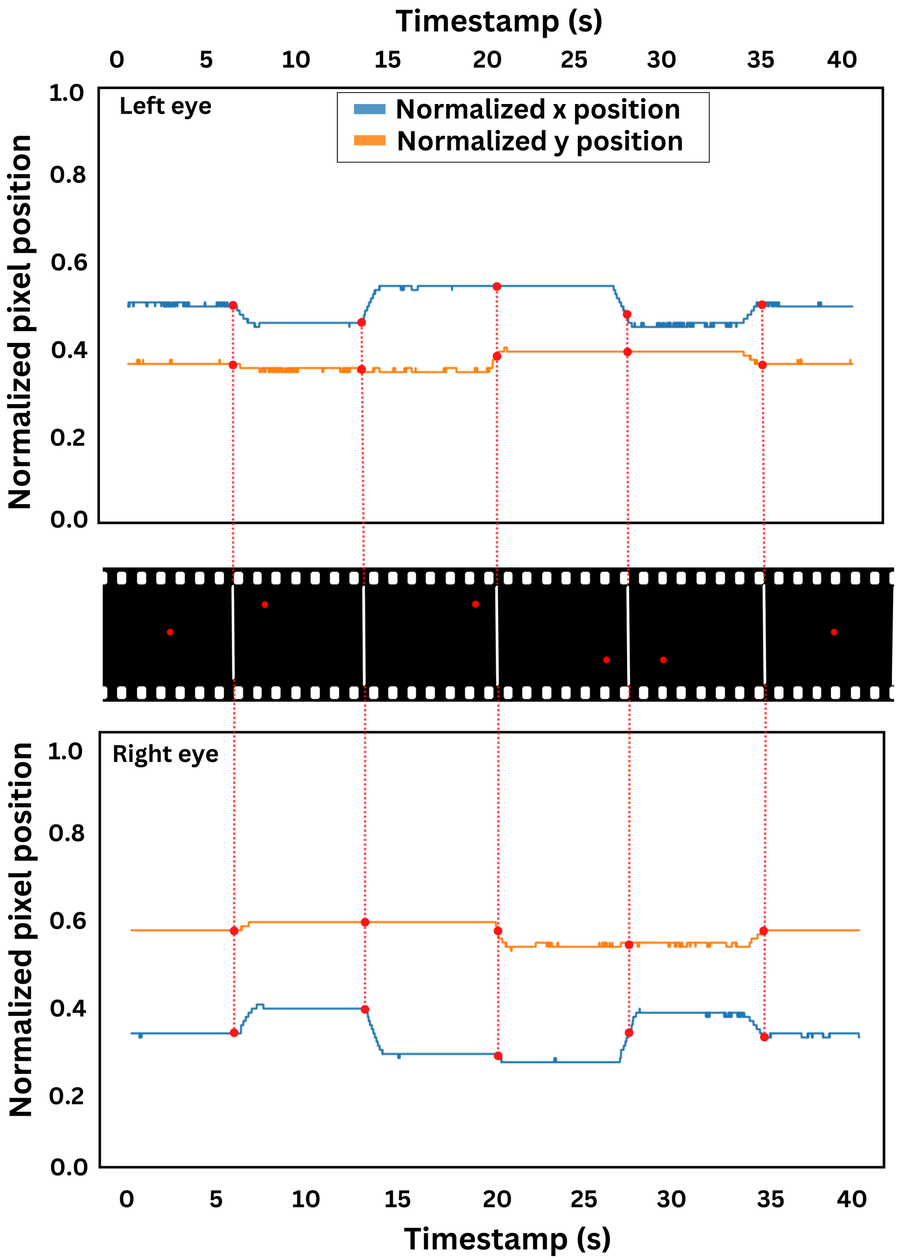

FIGURE 4.4. Pupil position vs time acquired recorded from an adult watching a video featuring a red ball that originates from the center of the screen and sequentially moves to each of the four corners, remaining stationary for a duration of 5 seconds at each location. The red dotted lines depict the synchronization between the displayed video frames and the corresponding pupil positions.

CHAPTER 5

Conclusion

The feasibility of the preliminary design of the headset and optics was validated through optical simulations, as discussed in Chapter 3. The results indicate promising outcomes in terms of diffraction limited spot size and wide field of view. In addition, the pupil tracking experiments conducted in Chapter 4 have confirmed the ability of the system to acquire a wide field of view by analyzing typical pupil movement characteristics. These initial feasibility and design validity experiments and studies pave the road for the execution and implementation of these ideas. The VR-based headset addresses the limitations of optical imaging by removing the need for mechanical head stabilization, thereby increasing accessibility to eye care for individuals with physical, mental, and developmental disabilities. Its portability not only enhances affordability but also reduces the dependence on dedicated space and trained professionals, enabling diagnosis even in remote areas of the world.

There are certain limitations of the design discussed in this thesis and they are as follows:

- **Spot size:** Although the simulations generate a diffraction-limited spot size at the retina along the optical axis, the spot size enlarges as it moves away from the optical axis. This phenomenon is likely attributed to the optical characteristics of the current eye model utilized in the simulation. To address this concern, we plan to incorporate the Navarro eye model, a widely recognized model in this domain, in future simulations to overcome the issue.
- **FOV improvement:** As mentioned in Chapter 3, the current design provides a large horizontal field of view but the range of vertical field of view is limited by the shape and dimensions of the FSM and the dichroic mirror chosen.
- **VR-based headset design:** In the preliminary design of the VR-based headset, as depicted in Figure 3.6, two compartments are shown where the bottom compartment accommodates the components that are usually found in a VR headset, such as the display

screen and relay lens, whereas the top compartment contains the optical components pertaining to our design, including the FSM, galvanometer, and objective lens. The intial design appears bulky and seems uncomfortable for the user to wear. Going forward, improvements will be made by reducing the form factor of components such as the FSM and galvanometer and optimizing the placement of components.

Despite the limitations of our preliminary work, which we have identified earlier, our research has produced promising results. To further advance our research, the next step would be to acquire OCT and SLO images using a table-top system and compare the results with those obtained from our optical simulations. In order to replicate our design on a table-top system, the pupil tracking camera, actuators, acquisition module, and light source will all be centrally controlled through LabView and hardware from National Instruments. This approach will allow us to better understand the feasibility of our design and identify potential areas for improvement in future iterations.

The final phase of the project involves transferring the system from a table-top to a VR-based headset configuration. The efficacy of the OCT and SLO system will be evaluated based on the results of the experiments carried out on participating individuals.

Bibliography

[1] James G. Ravin. Hermann von helmholtz: The power of ophthalmoscopy. In *Foundations of Ophthalmology*, pages 85–93. Springer International Publishing, 2017.

[2] Dan P. Popescu, Lin-P'ing Choo-Smith, Costel Flueraru, et al. Optical coherence tomography: fundamental principles, instrumental designs and biomedical applications. *Biophysical Reviews*, 3(3):155–169, August 2011.

[3] Seth R Flaxman, Rupert R A Bourne, Serge Resnikoff, et al. Global causes of blindness and distance vision impairment 1990–2020: a systematic review and meta-analysis. *The Lancet Global Health*, 5(12):e1221–e1234, December 2017.

[4] Peter Ackland, Serge Resnikoff, and Rupert Bourne. World blindness and visual impairment: despite many successes, the problem is growing. *Community Eye Health*, 30(100):71–73, 2017.

[5] World Health Organization et al. World report on vision. 2019.

[6] Rupert R A Bourne, Seth R Flaxman, Tasanee Braithwaite, et al. Magnitude, temporal trends, and projections of the global prevalence of blindness and distance and near vision impairment: a systematic review and meta-analysis. *Lancet Glob. Health*, 5(9):e888–e897, September 2017.

[7] Treatable or preventable vision loss - The International Agency for the Prevention of Blindness — iapb.org. `https://www.iapb.org/learn/vision-atlas/about/insights/data-and-evidence/treatable-or-preventable-vision-loss/`. [Accessed 10-Apr-2023].

[8] Roya Husainzada. Situation analysis of human resources in eye care in afghanistan. *Community Eye Health*, 20(61):12, 2007.

[9] Patricia M Kiely and Joseph Chakman. Optometric practice in australian standard geographical Classification–Remoteness areas in australia, 2010. *Clin. Exp. Optom.*, 94(5):468–477, September 2011.

[10] Suzanne Gilbert and Daksha Patel. Recruiting and distributing eye health workers. *Community Eye Health*, 31(102):45–47, 2018.

[11] Jacqueline Ramke, Clare E. Gilbert, Arier C. Lee, et al. Effective cataract surgical coverage: An indicator for measuring quality-of-care in the context of universal health coverage. *PLOS ONE*, 12(3):e0172342, March 2017.

[12] Nazaradden Ibrahim, Francisco Pozo-Martin, and Clare Gilbert. Direct non-medical costs double the total direct costs to patients undergoing cataract surgery in zamfara state, northern nigeria: a case series. *BMC Health Services Research*, 15(1), April 2015.

[13] Herrieth Mganga, Susan Lewallen, and Paul Courtright. Overcoming gender inequity in prevention of blindness and visual impairment in africa. *Middle East Afr. J. Ophthalmol.*, 18(2):98–101, April 2011.

[14] J van Splunder, J S Stilma, R M D Bernsen, and H M Evenhuis. Prevalence of visual impairment in adults with intellectual disabilities in the netherlands: cross-sectional study. *Eye*, 20(9):1004–1010, September 2005.

[15] Rufina T.Y. Chan and Maurice Yap. Access barriers to eye care utilization among people with physical disability in hong kong. *Procedia Environmental Sciences*, 36:46–49, 2016.

[16] Manjula Marella, Fleur Smith, Lukman Hilfi, and Deni Sunjaya. Factors influencing disability inclusion in general eye health services in bandung, indonesia: A qualitative study. *International Journal of Environmental Research and Public Health*, 16(1):23, December 2018.

[17] Ge Song, Kengyeh K. Chu, Sanghoon Kim, et al. First clinical application of low-cost OCT. *Translational Vision Science &amp Technology*, 8(3):61, June 2019.

[18] Helena Lee, Frank A. Proudlock, and Irene Gottlob. Pediatric optical coherence tomography in clinical practice—recent progress. *Investigative Opthalmology &amp Visual Science*, 57(9):OCT69, July 2016.

[19] Amar Pujari, Gunjan Saluja, Divya Agarwal, et al. Clinical role of smartphone fundus imaging in diabetic retinopathy and other neuro-retinal diseases. *Current Eye Research*, 46(11):1605–1613, July 2021.

[20] Devrim Toslak, Taeyoon Son, Muhammet Kazim Erol, et al. Portable ultra-widefield fundus camera for multispectral imaging of the retina and choroid. *Biomedical Optics Express*, 11(11):6281, October 2020.

[21] Diego R. Palacios, Kai Shen, Sarfaraz Baig, et al. Wide field of view handheld smart fundus camera for telemedicine applications. *Journal of Medical Imaging*, 8(02), March 2021.

[22] Jamie Ikeda, Bradley V. Davitt, Monica Ultmann, et al. Brief report: Incidence of ophthalmologic disorders in children with autism. *Journal of Autism and Developmental Disorders*, 43(6):1447–1451, February 2012.

[23] Robert A. Avery, Eugene I. Hwang, Hiroshi Ishikawa, et al. Handheld optical coherence tomography during sedation in young children with optic pathway gliomas. *JAMA Ophthalmology*, 132(3):265, March 2014.

[24] Mark Draelos, Pablo Ortiz, Ruobing Qian, et al. Contactless optical coherence tomography of the eyes of freestanding individuals with a robotic scanner. *Nature Biomedical Engineering*, 5(7):726–736, July 2021.

[25] Krzysztof Krysta, Marek Krzystanek, Wiesław J Cubała, et al. Telepsychiatry and virtual reality an the teatment of patients with intellectual and developmental disabilities. *Psychiatr. Danub.*, 29(Suppl 3):656–659, September 2017.

[26] Patricia Mesa-Gresa, Hermenegildo Gil-Gómez, José-Antonio Lozano-Quilis, and José-Antonio Gil-Gómez. Effectiveness of virtual reality for children and adolescents with autism spectrum disorder: An evidence-based systematic review. *Sensors*, 18(8):2486, August 2018.

[27] D Purves, G J Augustine, D Fitzpatrick, et al. Anatomy of the eye. *Neuroscience*, 2001.

[28] Helga Kolb. Simple anatomy of the retina. In *Webvision: The Organization of the Retina and Visual System*. University of Utah Health Sciences Center, Salt Lake City (UT), 1995.

[29] Robert N. Weinreb, Christopher K. S. Leung, Jonathan G. Crowston, et al. Primary open-angle glaucoma. *Nature Reviews Disease Primers*, 2(1), September 2016.

[30] Michael D. Abràmoff, Mona K. Garvin, and Milan Sonka. Retinal imaging and image analysis. *IEEE Reviews in Biomedical Engineering*, 3:169–208, 2010.

[31] Robert N. Weinreb, Tin Aung, and Felipe A. Medeiros. The pathophysiology and treatment of glaucoma. *JAMA*, 311(18):1901, May 2014.

[32] Laurence S Lim, Paul Mitchell, Johanna M Seddon, et al. Age-related macular degeneration. *The Lancet*, 379(9827):1728–1738, May 2012.

[33] Ursula Schmidt-Erfurth, Victor Chong, Anat Loewenstein, et al. Guidelines for the management of neovascular age-related macular degeneration by the european society of retina specialists (euretina). *British Journal of Ophthalmology*, 98(9):1144–1167, 2014.

[34] Wei Wang and Amy Lo. Diabetic retinopathy: Pathophysiology and treatments. *International Journal of Molecular Sciences*, 19(6):1816, June 2018.

[35] Rui Bernardes, Pedro Serranho, and Conceição Lobo. Digital ocular fundus imaging: A review. *Ophthalmologica*, 226(4):161–181, 2011.

[36] Michael D. Abramoff, Mona K. Garvin, and Milan Sonka. Retinal imaging and image analysis. *IEEE Reviews in Biomedical Engineering*, 3:169–208, 2010.

[37] C. Richard Keeler. 150 years since babbage's ophthalmoscope. *Archives of Ophthalmology*, 115(11):1456, November 1997.

[38] Harold R. Novotny and David L. Alvis. A method of photographing fluorescence in circulating blood in the human retina. *Circulation*, 24(1):82–86, July 1961.

[39] Mikael Häggström. Medical gallery of mikael häggström 2014. *WikiJournal of Medicine*, 1(2), 2014.

[40] Won June Lee, Ji Hong Kim, Yong Un Shin, et al. Differences in eye movement range based on age and gaze direction. *Eye*, 33(7):1145–1151, March 2019.

[41] Rod Watkins. Opticstudio models of the human eye – knowledgebase, Mar 2021.

[42] Isabel Escudero-Sanz and Rafael Navarro. Off-axis aberrations of a wide-angle schematic eye model. *Journal of the Optical Society of America A*, 16(8):1881, August 1999.